þÿ Synthesis of N-Doped Magnetic WO3 x@Mesopor Using a Diatom Template and Plasma Modification : Visible-Light-Driven Photocatalytic Activities

Gholami, Peyman

2021-03-24

Gholami , P , Khataee , A , Bhatnagar , A & Vahid , B 2021 , ' Synthesis of N-Doped þÿ Magnetic WO3 x@Mesoporous Carbon Using a Diatom Template and Pla : Visible-Light-Driven Photocatalytic Activities ' , ACS Applied Materials & Interfaces , vol. 13 , no. 11 , pp. 13072-13086 . https://doi.org/10.1021/acsami.0c21076

http://hdl.handle.net/10138/341620
https://doi.org/10.1021/acsami.0c21076

Synthesis of N-Doped Magnetic WO_{3-x}@Mesoporous Carbon using Diatom Template and Plasma Modification: Visible-Light-Driven Photocatalytic Activities

Peyman Gholami, [a,b,c] Alireza Khataee, [a,d,*] Amit Bhatnagar, [b,e] Behrouz Vahid [f]

[a] Research Laboratory of Advanced Water and Wastewater Treatment Processes, Department of Applied Chemistry, Faculty of Chemistry, University of Tabriz, 51666-16471 Tabriz, Iran

[b] Department of Environmental and Biological Sciences, University of Eastern Finland, P.O. Box 1627, FI-70211 Kuopio, Finland

[c] Department of Chemistry, University of Helsinki, P.O. Box 55, Helsinki 00014, Finland

[d] Peoples' Friendship University of Russia (RUDN University), 6 Miklukho-Maklaya Street, Moscow, 117198, Russian Federation

[e] Department of Separation Science, LUT School of Engineering Science, LUT University, Sammonkatu 12, FI-50130, Mikkeli, Finland

[f] Department of Chemical Engineering, Tabriz Branch, Islamic Azad University, Tabriz, Iran

* Corresponding author:

a_khataee@tabrizu.ac.ir

Abstract

Synthesis of 3D photocatalysts offers great potential for chemical conversion and hydrogen generation as appropriate solutions for environmental protection and energy shortage challenges. In this study, the magnetic WO_{3-x}@mesoporous carbon (M-WO_{3-x}@MC) was synthesized through evaporation-induced self-assembly (EISA) method applying diatom frustules as a natural template. Then, plasma modification was used to prepare the N-doped M-WO_{3-x}@MC (NM-WO_{3-x}@MC) with enhanced photocatalytic activity and durable performance. The WO_{3-x} was embedded in the conductive MC, which was also partially reduced by the carbon precursor within the heat-treatment procedure. The obtained M-WO_{3-x}@MC was treated by the plasma under N_2 atmosphere for the production of the final photocatalyst containing both the N-doped WO_{3-x} and MC. As a result, the NM-WO_{3-x}@MC had larger surface area (208.4 m^2 g^{-1}), narrower band gap (2.3 eV), more visible light harvesting and confined electron-hole pairs recombination. The H_2 generation rates of net WO_3 nanorods and NM-WO_{3-x}@MC nanocomposite were estimated as 532 and 2765 μmol g^{-1} h^{-1}, respectively. Additionally, more than 90% of antibiotics (cephalexin, cefazolin and cephradine) degradation and 76% of total organic carbon (TOC) elimination were obtained after 120 and 240 min of photocatalytic process under visible light irradiation. Eventually, more than eight intermediates were detected for each antibiotic degradation using the GC-MS method and based on the obtained results, the possible degradation pathways were suggested.

Keywords: Reduced tungsten oxide; Plasma modification; WO_{3-x}@mesoporous carbon; Nitrogen doping; Hydrogen evolution; β-lactam antibiotics degradation.

1. Introduction

Release of toxic pollutants in the environment, as well as a considerable enhancement of non-renewable energy usage, occur as a result of rapid urbanization and industrialization [1, 2]. To confront the environmental issues and increase the utilization of renewable energy sources, photocatalytic generation of hydrogen (H_2) has attained remarkable consideration [1, 3]. Furthermore, contamination of water resources, due to the considerable misuse of emerging pollutants (such as antibiotics, hormones, endocrine-disrupting compounds, surfactants, etc.), has become a serious menace to human beings and the ecological environment [4]. Especially, β-lactam antibiotic residues from humans or livestock medicines, hospital effluent and aquaculture are extensively found in the environment. Observation of antibiotic-resistant pathogens, carcinogenic influences in the ecological environment and toxic complex production with metal ions are the main damages related to long-term misuse of antibiotics [5, 6]. Adsorption and biological treatment are not suitable processes for antibiotics removal due to secondary waste formation and their biotoxicity [5, 6]. Consequently, it is needed to apply promising methods for the efficient treatment of biotoxic contaminants.

Photocatalysis as a green and environmentally-friendly technology relies on its benefits like low cost, straightforward processing and ecological protection [7]. It is common to excite the photocatalysts by ultraviolet (UV) irradiation comprising only 3–5% of sunlight owing to their high band gaps [8]. Hence, their usages are confined from practical point of view and accordingly, developing nanomaterials with an adequate response to visible light has great priority [8]. N-type tungsten trioxide (WO_3, energy band gap (E_g) ~2.8 eV) can be excited by solar or domestic indoor irradiations demonstrating reinforceable visible light excitement [9, 10]. Its proper features including stability, nontoxicity, physicochemical behavior and low-cost make WO_3 a suitable material with diverse applications. However, the net WO_3 has inadequate reduction potential and instant charge carriers recombination, which leads to slight energy conversions [9, 10]. The

WO_3 photocatalytic activity has been improved using helpful approaches including the formation of binary and ternary composite nanomaterials, doping with non-metals and metals, modification of catalysts surface and sensitization with dyes [9-12]. Besides, a vacancy of oxygen in the WO_{3-x} provides a shallow donor to enhance the conductivity and adsorption of various substances [12, 13].

The photocatalysts synthesis with desired morphology and nano-sized structure confronts significant aggregation/agglomeration obstacles. To prevail this problem, a practicable method is needed to form the three-dimensional (3D) structures with controllable sizes and morphologies [12, 14]. For instance, natural templates can be applied for this purpose like single-cell diatoms to prepare required 3D structures [14]. The diatoms with 3D silica cell wall (frustule) supply complex and ordered pore design, which cannot be produced by the existing synthesis procedures [14].

Carbon-supported photocatalysts can be doped by the nitrogen atoms due to their notable electron affinity to adjust the electrical and optical properties of the semiconductors [15, 16]. Different synthesis procedures have been described with various N-dopant sources including direct amination by triethylamine, solvothermal method using guanidine carbonate, sol-gel process using urea and photocatalyst precursor treatment with triethylamine/ethanol in supercritical conditions [17]. Moreover, N atoms can be incorporated into the semiconductors lattice [18], graphene [19] and metal gate materials [20] efficiently by practical N_2 plasma exposure.

Preparation of the magnetic WO_{3-x}/mesoporous carbon (M-WO_{3-x}@MC) and its doped form with the nitrogen (NM-WO_{3-x}@MC) using the non-thermal plasma can resolve the above-mentioned drawbacks. The as-synthesized Z-scheme photocatalyst not only possesses enhanced harvesting of light, but also intensifies the transportation of electrons, decreases the recombination rate of electron-holes and enhances the WO_3 contact with the reactants. To the

best of our knowledge, there is no report on the fabrication of such high-performance and stable nanocomposite using diatom template and plasma modification. Hence, the aim of this study was the integration of mesoporous carbon and nitrogen heteroatoms with partially reduced tungsten trioxide to produce the NM-WO_{3-x}@MC nanostructures. Then, the photocatalytic degradation of antibiotics and H_2 production were investigated using the recoverable catalyst. The synthesis of the photocatalyst was proved according to the results attained from detailed characterization and the role of each component and plasma modification were explained elaborately. Moreover, a plausible mechanism of the photo-generated charge carriers transfer was suggested for the antibiotics degradation and photocatalytic H_2 production based on the results of electron spin resonance (ESR), linear sweep voltammetry (LSV) and free radical scavenger suppression experiments.

2. Materials and methods

2.1. Reagents and chemicals

Iranian Biological Resource Center (Iran) provided the diatom cells. Sodium hydroxide (NaOH, ≥ 98%), ferrous sulfate tetrahydrate ($FeSO_4.4H_2O$, 99%), N-hydroxysuccinimide (NHS), ammonium formate (NH_4HCO_2, 99.9%), ethanol (C_2H_5OH, 99%), sulfuric acid (H_2SO_4, ≥ 98%), dimethylsulfoxide (DMSO), sodium sulphate (Na_2SO_4, 99.9%) diethyl ether ($C_4H_{10}O$, ≥ 99.7%), *meso*-2,3-dimercaptosuccinic acid (DMSA), hydrogen peroxide (H_2O_2, 30%), ferric chloride hexahydrate ($FeCl_3.6H_2O$, ≥ 98%), ferrous chloride tetrahydrate ($FeCl_2.4H_2O$, ≥ 99%), N,O-bis-(trimethylsilyl)-acetamide ($C_8H_{21}NOSi_2$, ≥ 95%) and hydrochloric acid (HCl, 38%) were supplied from Merck (Germany). Formaldehyde solution (CH_2O, 37 wt%), phenol (C_6H_5OH, ≥ 99%), 1-ethyl-3-(3- dimethylaminopropyl) carbodiimide ($C_8H_{17}N_3$, ≥ 99%), isopropyl alcohol ($(CH_3)_2CHOH$, 99.5%), acetic acid (CH_3CO_2H, ≥99.8%),

benzoquinone ($C_6H_4O_2$, ≥ 98%), tetrahydrofuran (THF, C_4H_8O ≥ 99%), acetone (C_3H_6O, 99.8%), isopropanol (C_3H_8O, 99%), tungsten chloride (WCl_6, 99.9%) and ethylenediaminetetraacetic acid disodium salt (EDTA-Na_2, $C_{10}H_{14}N_2Na_2O_8$, 99%) were obtained from Sigma-Aldrich (USA). Cephalexin, cefazolin and cephradine were purchased via Loghman Co. (Iran).

2.2. Synthesis of materials

2.2.1. Diatom cells preparation

To prepare nanoporous silica, the organic matrix coating the wall of diatom was eliminated by applying the H_2O_2/Fe^{2+} (Fenton) process accompanied with ultrasound assistance, which was explained concisely [21]. Briefly, $FeSO_4.4H_2O$ (15 mM) and H_2O_2 (60 mM) were added into an aqueous suspension (80 mL) of the cells (48×10^4 cells mL^{-1}). NaOH (0.1 M) and H_2SO_4 (0.1 M) solutions were used to adjust the pH of the suspension to 3. Then, the suspension was placed in the exposure of the ultrasound irradiation at 40 °C for 4 h employing an ultrasonic bath (300 W, 40 kHz, EP S3, Sonica, Italy). The obtained cells were centrifuged at 4500 rpm for 15 min to separate them from the liquid phase. Finally, the gathered powder with white color was washed first with the NH_4HCO_2 (0.5 M) and then with deionized H_2O followed by drying at 10 ˚C for a day.

2.2.2. Fe_3O_4 nanoparticles preparation

The co-precipitation method at alkaline conditions was used for the synthesis of Fe_3O_4 nanoparticles (NPs). Briefly, $FeCl_2.4H_2O$ (3.33 g) and $FeCl_3.6H_2O$ (9.10 g) were stirred in a three-neck round-bottom vessel containing 400 mL of the water under an inert atmosphere at room temperature for 20 min. In order to obtain Fe_3O_4 NPs, the pH was increased to 12 by

adding ammonia (94 mL) to the solution with vigorous mixing. The resulted black precipitate was centrifuged at 5000 rpm for 2 min and washed to eliminate the unreacted ions, which eventually dried under vacuum condition (12 h) [22]. The Fe_3O_4 NPs (20 mg) were modified in the toluene (2 mL) by adding the DMSA (20 mg) and DMSO (2 mL) solutions. The prepared solution was stirred at 25 °C (12 h) and the formed precipitant was washed with the ethyl acetate. Finally, the DMSA-Fe_3O_4 NPs were collected using a magnetic bar and stored in the water [22].

2.2.3. Magnetic diatom frustules preparation

The mixture of an aqueous solution of Fe_3O_4 NPs (0.6 g/L, 100 mL), NHS (0.3 g), 1-ethyl-3-(3-dimethylaminopropyl) carbodiimide (0.3 g) and treated diatom frustules (0.1 g) was prepared and mixed at 25 °C for 48 h to produce magnetic diatom frustules, which afterward centrifuged and washed by the Milli-Q water.

2.2.4. Synthesis of resol precursor

A solvable resol was prepared from formaldehyde and phenol polymerization as elaborated elsewhere [23, 24]. Concisely, the melted phenol (6.10 g) was added dropwise to the NaOH solution (1.30 g, 20%) and mixing for 10 min. Afterward, formaldehyde solution (10.0 g, 37%) was poured into the mixture dropwise and stirred at 75 °C for 1 h. Next, it was cooled to room temperature, followed by the addition of HCl (2.0 M) to achieve pH 7.0. Finally, the aqueous solution was evaporated in the vacuum at 45 °C and the obtained yield was maintained in the THF (20%).

2.2.5. Synthesis of magnetic WO_{3-x}@mesoporous carbon applying diatom template

Magnetic WO_{3-x}@mesoporous carbon (M-WO_{3-x}@MC) was prepared through one-pot evaporation-induced self-assembly (EISA) procedure as follows [23, 24]: A suspension containing the magnetic diatom frustules (0.1 g) and acetone (20 mL) was mixed with the prepared carbon precursor (0.1 g resol, 20 wt% in THF) and WCl_6 (0.13 g), which then stirred severely for 10 min. The obtained suspension was sonicated (2 h) after adding anhydrous ethanol (0.25 mL). The resulted mixture was concentrated (50 °C, 8 h), and then, it was dried (100 °C, 8 h). Afterward, the remaining solid was calcined (700 °C, 2 h) under the nitrogen atmosphere. Eventually, the as-prepared nanocomposites were placed in the HF (10 wt%) for one day to eliminate the silica cores. It should be noted that the WO_3 nanorods were attained by the identical method without the diatom cells and resol precursor addition.

2.2.6. Nitrogen doping

Plasma reactor, which consists of a Pyrex tube equipped with two aluminum electrodes was utilized for the N-dopping of M-WO_{3-x}@MC particles. The N_2 gas was fed to the plasma reactor (5 cm^3/s) by rotary and turbo-molecular pumps to reach 50 Pascal pressure. The non-thermal plasma was generated by supplying the high-voltage (1200 V) and direct current (DC) using a DC power source. A Schematic illustration of the preparation of NM-WO_{3-x}@MC nanocomposite is shown in Fig. S1.

2.3. Characterization

The phase purity and crystal structure of the materials were investigated by a Bruker D8 (Germany) diffractometer with Cu Ka radiation functioned at 40 kV. The morphologies of the materials were investigated using a JEM-2100F transmission electron microscope (TEM,

JEOL, Japan) and a Zeiss Sigma HD VP scanning electron microscope (SEM, Zeiss NTS, Cambridge, UK) with an energy-dispersive x-ray spectroscopy (EDS) analyzer. The diameter size distributions for diatom frustules pores, Fe_3O_4 nanoparticles and WO_{3-x} nanorods were measured using Microstructure Distance Measurement software (Nahamin Pardazan Asia Co., Iran). Raman measurements were carried out by Ntegra Spectra spectrometer (NT-MDT, Russia) with 532 nm laser excitation. The textural properties of the catalysts were examined by performing N_2 adsorption-desorption experiments using Micromeritics 3Flex (USA) analyzer at 77 K. Barrett–Joyner–Halenda (BJH) and Brunauer-Emmett-Teller (BET) methods were applied to evaluate pore size distribution, BET specific surface area (S_{BET}) and total pore volume. A Thermo Fisher Scientific Escalab 250Xi (USA) spectrometer with a monochromatic Al Kα radiation (1486.6 eV) was used to collect X-ray photoelectron spectra (XPS). Valence band X-ray photoelectron spectroscopy (VB-XPS) with an energy step of 0.1 eV was also performed by the same equipment. The 5,5-dimethyl-1-pyrroline N-oxide (DMPO) spin trapping ESR spectra were recorded on a Bruker ESR 300E spectrometer (Germany).

2.4. Optical and electrochemical tests

The electrochemical studies were carried out by an Autolab potentiostat/galvanostat instrument (PGSTAT128N, Metrohm, Netherlands). For fabrication of work electrode, photocatalyst (40 mg) was blended with Nafion (5%, 200 μL) and ethanol (800 μL), then ultrasonically dispersed (3 h). The obtained suspension was dip-coated on a clean glassy carbon electrode (GCE, 1 × 1 cm^2) with 0.07 cm^2 geometric area and dried at room temperature. Platinum (Pt) and saturated calomel electrode (SCE) were operated as the counter and reference electrodes, respectively. The LSV was conducted at 10 mV s^{-1} scan rate. Electrochemical impedance spectra (EIS) were plotted at 200 mV overpotential against normal hydrogen electrode (NHE) with 5.0 mV amplitude and the range of frequency from 0.01 to 100

Hz in the Na_2SO_4 solution (0.5 M). A Perkin Elmer LS45 spectrometer (USA) was used to record the photoluminescence (PL) spectra. The absorption characteristics of the samples were studied by an Ultraviolet-visible diffuse reflectance spectrophotometer (UV-Vis DRS, UV–3700, Shimadzu, Japan).

2.5. Test of photocatalytic performance for H_2 generation

The tests for photocatalytic H_2 generation were performed in a Pyrex flask (100 mL) at ambient conditions. Briefly, a photocatalyst (50 mg) was added into the Na_2SO_3 (0.25 M) and Na_2S (0.35 M) solution (80 mL), then the mixture was sonicated (1 h). Afterward, the N_2 gas was used for degassing the obtained mixture for 0.5 h to gain the anaerobic state. A LED lamp (300 W, $\lambda \geq 420$ nm, Shenzhen StarVanq Technology, China) acted as the visible light source. Through the run, the mixture was stirred by a magnetic bar to maintain the photocatalyst in the suspension. A gas chromatography instrument (Agilent Technologies 7890A, TCD) was applied to analyze the generated H_2. The apparent quantum efficiency (AQE) was evaluated using the following equation [25]:

$$AQE\ (\%) = \frac{2 \times the\ number\ of\ evolved\ H_2\ molecules}{the\ number\ of\ incident\ photons} \times 100\ = \frac{2 \times r_{H2} \times L}{\frac{I\lambda}{hc}} \times 100 \qquad (1)$$

where r_{H2} is the evolved H_2 per second in molar amount, L is the Avogadro constant, I is the power of incident light, λ is the wavelength of irradiation, h is the Planck constant, and c is the light speed.

2.6. Test of photocatalytic activity for antibiotics degradation

Cephalexin, cefazolin and cephradine were selected as model pollutants to evaluate the photocatalytic activity of the as-synthesized catalysts for photodegradation of β-lactam antibiotics in the contaminated water. In general, a photocatalyst (60 mg) was dispersed into 100 mL of antibiotics solution (concentration of each compound = 2 mM) and the mixture was

agitated (0.5 h) in dark condition to achieve the equilibrium of adsorption-desorption. Subsequently, the LED lamp was switched on and the mixture was placed in the exposure of the visible light. Within the photocatalytic process, 1.0 mL of the antibiotics solution was withdrawn at distinct intervals of time and then the photocatalyst particles were separated from the treated solution using a magnet. The antibiotics degradation efficiencies were monitored using an HP-1090 Series II liquid chromatography (USA), equipped with a UV detector. Just prior to determining the concentration of the pollutants, the antibiotics solution containing sodium chloride (1%) in the MQ water (1 + 9) was prepared as the working solution. The aqueous mobile phase consisted of acetic acid (10%) in the water-isopropyl alcohol-water (4 + 9 + 87) and the flow-rate was set at 1.0 mL min^{-1}. The system was equipped with 4.6 × 250 mm C18 reversed-phase column. After trying different wavelengths (235, 240, 247, 250, and 255 nm), the optimal analytical wavelength for the studied β-lactam antibiotics was found to be 247 nm, since both high sensitivity and good chromatographic response were obtained at this wavelength [26]. Fig. S2 shows the separation chromatogram of the antibiotics using the explained method. The retention time of the cefazolin, cephalexin and cephradine were appeared at 2.8, 4.5 and 7.3 min, respectively. Table S1 presents the calibration data for each antibiotic; high linear correlation coefficients ($R^2 \geq 0.9971$) demonstrate that the proposed method offers a reasonable precision for the simultaneous determination of β-lactam antibiotics in the range of 0.2-4.0 mM. Degradation by-products were recognized by Agilent 6890 gas chromatography (GC, Canada) combined with Agilent 5973 mass spectrometer (MS, Canada), which had a capillary column of TG-5MS. The elaborated explanation for the sample preparation and intermediates identification has been presented elsewhere [27]. The total organic carbon concentration was measured by a TOC analyzer (multi N/C 2100S, Analytik Jena, Germany). The concentration of anions was determined by a DIONEX ICS-2100 ion chromatography (IC) system (ThermoFisher, USA).

3. Results and discussion

3.1. Morphological and structural characteristics of the catalysts

Fig. 1 (a) and (b) demonstrates that before treating the diatom cells, impurities covered the frustules. with a disk-like morphology (~7 μm outer diameter). The ultrasound-assisted H_2O_2/Fe^{2+} procedure [21] was applied to eliminate them and to prepare the treated diatom frustules, which can be seen in Fig. 1 (c) and (d). The prepared frustules have an ordered porous structure with controlled nano-pores size (10-20 nm), which are uniformly spread on the walls of cell. Fig. 1 (e) and (f) reveal the proper stabilization of Fe_3O_4 NPs on the frustule surface. As can be seen from the SEM images of NM-WO_{3-x}@MC (Fig. 1 (g) and (h)), this nanocomposite possesses almost a similar shape (disk-like) and the diameter with the diatom template even after its elimination. It is concluded that the diatom template surface is firstly coated with WO_{3-x}@MC and the 3D morphology of the prepared nanostructure is not changed after the template elimination by the HF. A homocentric growth occurred, which led to the hierarchical 3D nanostructures with a hole in its center by the EISA method. Based on the SEM images, pore diameter size of diatom frustules (Fig. S3 (a)), diameter size of Fe_3O_4 nanoparticles (Fig. S3 (b)) and WO_{3-x} nanorods (Fig. S3 (c)), were measured to be in the ranges of 10–22 nm, 10–40 nm and 14-26 nm, respectively.

The EDS spectra of the samples were illustrated in Fig. S4 (a-d). The treated and untreated frustules have similar elements including oxygen, carbon, calcium and silicon. The elimination of organic materials from the frustule surface results in a remarkable decrease in the carbon peak intensity, and a vice versa trend is observed for the peak of silicon; it is clearly owing to the diatom frustule purification, which mainly consisted of silica. Moreover, extra peaks related to the Fe are observed in the EDS spectra of magnetic frustules due to the presence of Fe_3O_4 (Fig. S4 (c)). Eventually, the EDS of NM-WO_{3-x}@MC has a strong peak related to the W as well as the peaks assigned to O and C beside the N peak, which confirms the proper

nanocomposite synthesis using the prepared magnetic template [21]. It can also be concluded that nitrogen was appropriately introduced into the catalyst structure after the plasma modification.

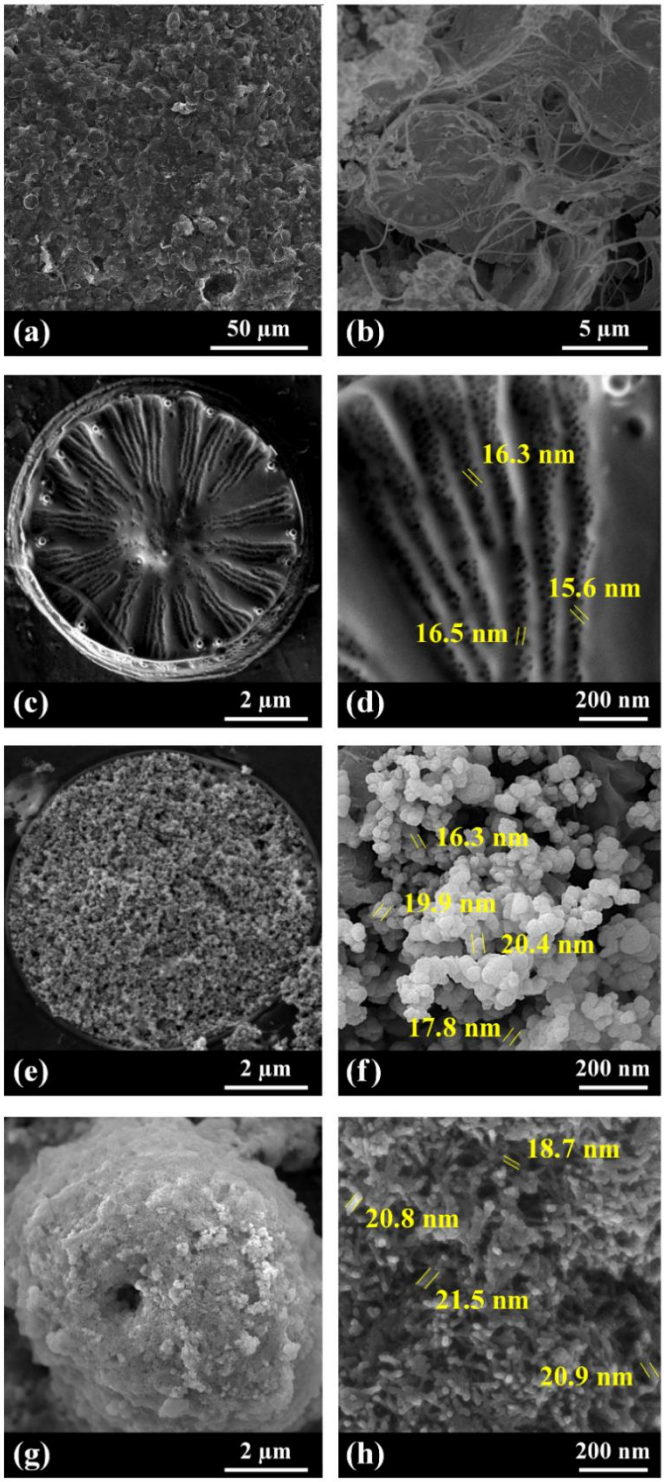

Fig. 1. SEM images of untreated frustule (a and b), treated frustule (c and d), magnetic frustule (e and f) and NM-WO_{3-x}@MC nanocomposite (g and h).

Further investigations were carried out using the high-resolution TEM (HRTEM) to obtain further data for the structural and morphological properties of the prepared samples including WO_3 nanorods, Fe_3O_4 nanoparticles, M-WO_{3-x}@MC and NM-WO_{3-x}@MC nanocomposites. Uniform morphology of WO_3 nanorods with a length of ≤ 120 nm and diameter of ≤ 20 nm are seen in Fig. 2 (a and b); the ~0.383 and ~0.372 nm interplanar distances between the regular lattice fringes are attributed to the (002) and (020) planes of hexagonal WO_3 crystal [Fig. 2 (b)] [28]. Moreover, Fe_3O_4 nanoparticles display an appropriate dispersity with spherical morphology [Fig. 2 (c) and (d)]; the ~0.293 nm interplanar distance between the common lattice fringes is related to the (220) crystal plane of the Fe_3O_4 [Fig. 2 (d)] [29]. Besides, TEM images of M-WO_{3-x}@MC [Fig. 2 (e) and (f)] show that tungsten oxide is uniformly and completely embedded into the MC. Eventually, a rougher surface was observed for the NM-WO_{3-x}@MC [Fig. 2 (g) and (h)] due to the etching effect of plasma, which is the effective surface treatment method. The plasma with highly energy species can also etch the carbon-based substances generating controllable defects [30]; the extra ~0.382 nm interplanar spacing attributed to (010) $WO_{2.9}$ plane confirmed its partially reduction, which is incorporated in the carbon [31].

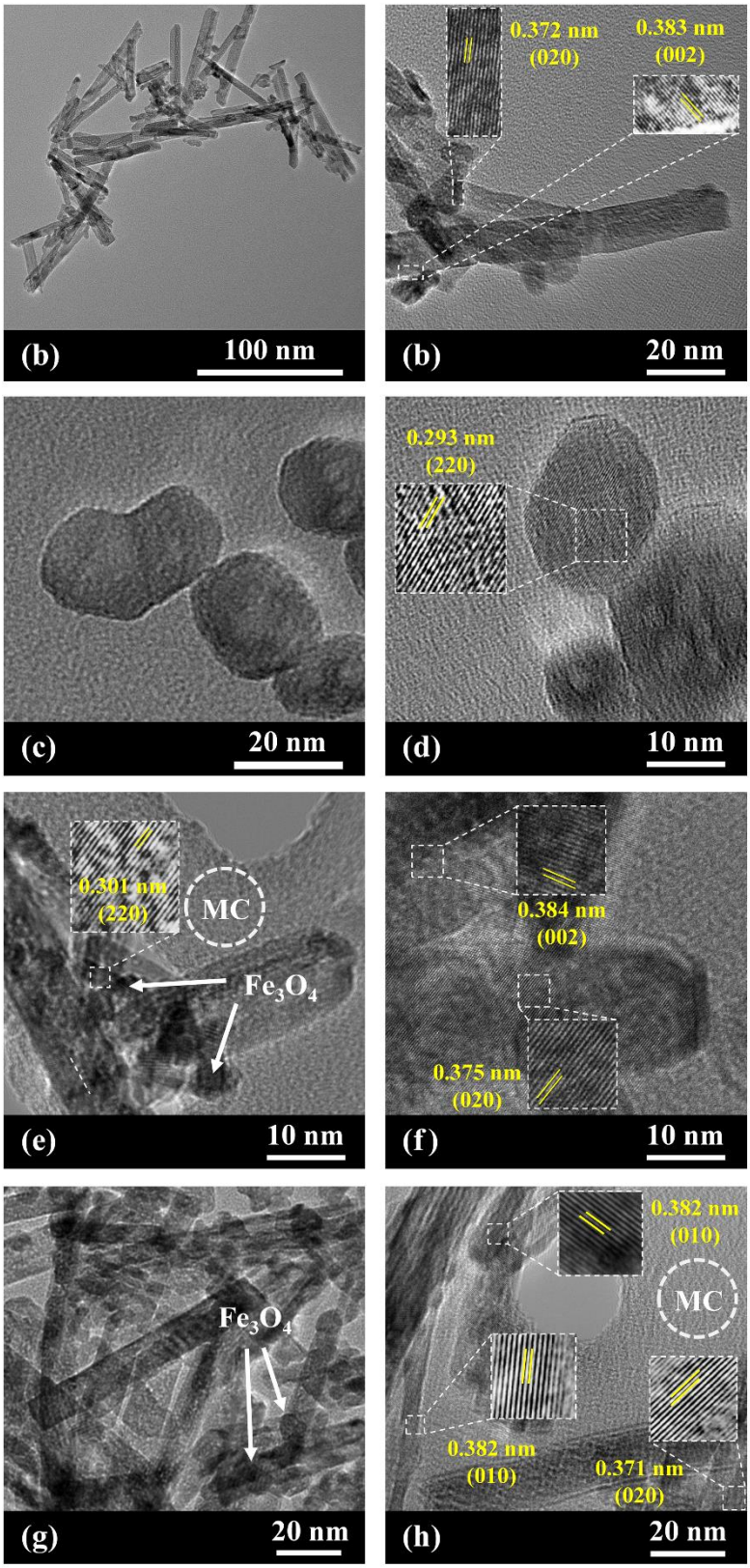

Fig. 2. TEM and HRTEM images of WO_3 nanorods (a and b), Fe_3O_4 nanoparticles (c and d), M-WO_{3-x}@MC (e and f) and NM-WO_{3-x}@MC (g and h) nanocomposites.

Structural and crystallinity properties of the prepared samples including the diatom frustules, WO_3, M-WO_{3-x}@MC and NM-WO_{3-x}@MC were investigated by the XRD analyses, which are displayed in Fig. 3 (a). The XRD plot of diatom frustules demonstrates no sharp peaks, proving its amorphous structure; the peak in the range of 13.5° to 29.5° is related to the amorphous silica [32], which is commonly observed in the diatoms structures [33]. The XRD patterns confirm the preparation of Fe_3O_4 and WO_3 based on the diffraction peaks at $2\theta = 30.1$, 35.7, 43.2, 54.2, 57.3, and 63.0° (JCPDS card 19-0629) and $2\theta = 13.7$, 22.8, 24.1, 26.6, 28.1, 33.3, 36.4, 46.4, and 57.2° (JCPDS No. 75-2187), respectively [23, 34]. The parameters of the unit cell for the prepared WO_3 were determined as a = 7.279 Å and c = 3.899 Å, which are in proper agreement with the hexagonal WO_3 specifications [35]. The XRD patterns of prepared nanocomposites including the M-WO_{3-x}@MC and NM-WO_{3-x}@MC have a sharp peak at ~25°, further peaks located at 54.9°, 48.2°, and 42.5°and the peaks related to the Fe_3O_4 compared to the pure WO_3. The peaks centered at ~25° and 42.5° are assigned to the (002) and (100) planes of the graphite (JCPDS No. 08-0415) confirming the generation of the MC via the resol addition during the procedure of nanocomposite materials synthesis [36]. Moreover, the extra peaks observed at 48.2° and 54.9° are related to (220) and (310) planes of the $WO_{2.9}$ (JCPDS No. 18-1417), verifying the reduction function of the precursor in the synthesis method [37]. Debye-Scherrer formula was applied to calculate the mean crystalline sizes of tungsten oxide in the prepared WO_3, M-WO_{3-x}@MC and NM-WO_{3-x}@MC using the full width at half maximum (FWHM) of (200) plane, which was 23, 19 and 18 nm, respectively [38]. These data reveal that the magnetic diatom surface can function as a nucleation agent for the carbon precursor graphitization and the formation of tungsten oxide nanorods lead to the nanostructured material generation with the smaller crystalline size [39].

Surface electronic properties and elemental composition of the samples were studied using the XPS spectroscopy; the obtained XPS spectra and elemental compositions are shown in Fig.

3 (b) and Table S2, respectively. The WO_3 has C=15 at%, W=19 at% and O=66 at% in its composition; the M-WO_{3-x}@MC and NM-WO_{3-x}@MC have more carbon levels of 22 at% and 25 at% with Fe amount of 10 at% and 11 at%, respectively. Furthermore, the NM-WO_{3-x}@MC spectrum shows a peak at ~399.2 ± 0.1 eV compared to M-WO_{3-x}@MC, which is attributed to N 1s with atomic content of 1% [Fig. 3 (b)]. The major W part in the tungsten oxide composition has the 6+ oxidation state, which is confirmed by the W 4f high-resolution spectrum of WO_3, exhibiting the peaks at 37.7 ± 0.1 and 35.6± 0.1 eV related to 4f5/2 and 4f7/2, respectively [Fig. 3 (c)] [40]. On the other hand, extra peaks at 34.3 ± 0.1 and 36.6± 0.1 eV in the W4f curves of M-WO_{3-x}@MC and NM-WO_{3-x}@MC confirm the W^{5+} presence as well. These results are in good agreement with the data gained from the XRD analysis, which reveals the partial reduction of tungsten oxide with resol polymer during the EISA synthesis procedure [35, 40]. As shown in Fig. 3 (d), the N 1s spectrum is deconvoluted into three constituents, which are related to the graphitic nitrogen (402.3 ± 0.1 eV), pyrrolic nitrogen (400.2 ± 0.1 eV) and pyridinic nitrogen (398.6 ± 0.1 eV) [41]. Actually, as M-WO_{3-x}@MC was exposed to the reactive species, their interactions resulted in the nitrogen-doped nanocomposite material with graphitic, pyrrolic and pyridinic bonding configurations after nitrogen groups transformation and the rearrangement of structure [42]. Rybin et al. [41] proved that the graphene electronic structure is affected by the N doping, which leads to a shift of Fermi level of pure graphene. The N-doped graphene becomes an n-type semiconductor in the case of pyrrolic or graphitic N-bond types, in which the Fermi level shifts to conduction band; moreover, the N-doped graphene becomes a p-type semiconductor in case of pyridinic nitrogen impurities, in which the Fermi level shifts to valence band [41, 43].

Raman spectroscopy was also used to obtain more detailed electronic and structural properties of the samples [Fig. 3 (e)]. The peaks at 273 and 322 cm^{-1} are related to δ(O–W–O) bending modes and the peaks at 712 and 808 cm^{-1} are assigned to ν(O–W–O) stretching modes

[44, 45]. Besides, two broad bands are observed at 1350 (D-band) and 1595 (G-band) cm^{-1} in the NM-WO_{3-x}@MC spectrum; the former band is assigned to the A_{1g} vibration of carbon, and the latter band is attributed to the E_{2g} vibration of sp^2-bonded carbon [44, 45]; these results are in good agreement with those studied for WO_3 mesosponge@carbon [45]. The successful preparation of tungsten oxide embedded MC is also confirmed by the comparison of the Raman spectra for the pure WO_3 and synthesized nanocomposite materials.

Nitrogen adsorption-desorption isotherms of the prepared samples including WO_3, M-WO_{3-x}@MC and NM-WO_{3-x}@MC are shown in Fig. 4 (a). Based on the IUPAC classification, all of them demonstrate type IV isotherms with the obvious type H3 hysteresis loops, which is the characteristics of mesoporous materials [Fig. 4 (a)]. The observed results were investigated by the Barrett–Joyner–Halenda (BJH) and Brunauer–Emmett–Teller (BET) to obtain data about pore size distribution, total pore volume and specific surface area for the produced materials (Table S3). The peaks for distribution of pore size [Fig. 4 (b)] are placed at 11.9, 9.3, 6.2 nm for WO_3, M-WO_{3-x}@MC and NM-WO_{3-x}@MC, respectively. The lower total pore volume and S_{BET} for WO_3 are owing to its remarkable density. It is presumed that the density of reduced WO_3 in the M-WO_{3-x}@MC and NM-WO_{3-x}@MC nanocomposites is near to the density of WO_3 due to their similar shape and crystallinity with the WO_3, which is based on the results acquired from the HRTEM and XRD analyses. On the other hand, when WO_{3-x} is embedded into the MC, the total pore volume and S_{BET} increase considerably (Table S3). It is owing to the production of mesoporous nanostructures with high order yielded from the efficient carbonization, remaining lots of voids in the structure of carbon [46]. Furthermore, NM-WO_{3-x}@MC demonstrates superior textural properties than the M-WO_{3-x}@MC. Combined with the TEM results, defects induced by the plasma etching may cause a greater surface area and hence, active sites.

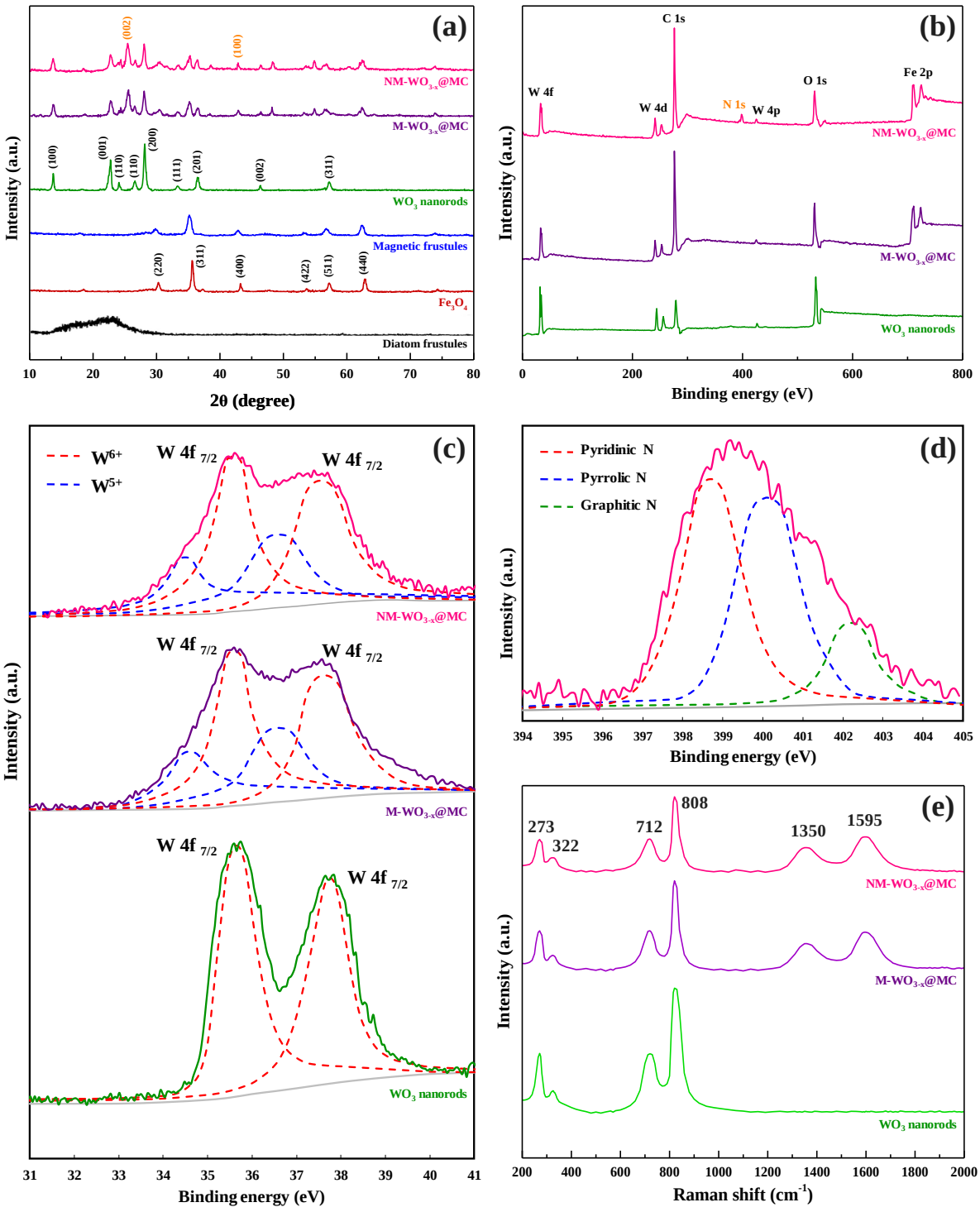

Fig. 3. XRD patterns (a), XPS full spectra (b), W 4f (c) and N 1s (d) high-resolution spectra and Raman spectra (e) of the samples.

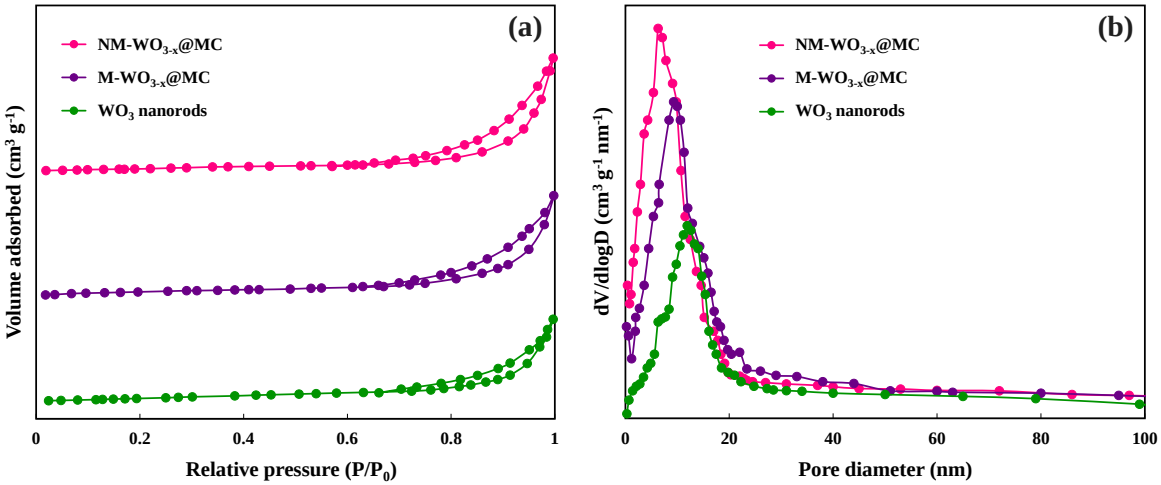

Fig. 4. N_2 adsorption-desorption isotherms (a) and pore size distributions (b) of WO_3 nanorods, M-WO_{3-x}@MC and NM-WO_{3-x}@MC nanocomposites.

The mechanism of the plasma modification to prepare NM-WO_{3-x}@MC could be concisely explained as follows: Ionized species had a substantial function for the implementation of the nitrogen doping in addition to the roughness enhancement of the photocatalyst surface. They could convey the energy, resulting in the CN bonding, which was in the excited state. The alteration in the modified photocatalyst surface could be related to the generation of volatile CN within the plasma procedure [47, 48]. It should be mentioned that the nitrogen plasma had a lower etching effect in comparison with other plasmas leading to the relative graphite phase stability in the etching process [49]. Furthermore, the nitrogen incorporation in the sp^3 structure could act as a bridge between sp^2 clusters, resulting in the π- and π*-bands localization that are in charge of the aromatic ring clusters [48]. Hence, these ionized species in the N_2 plasma caused the graphitic phase predominance compared to the amorphous one and consequently, hierarchical networks comprised of the aromatic ring clusters accumulated during the plasma modification gradually. According to the XPS results, N-including ions bond with carbon and nitrogen-doped MC is produced in the whole nanocomposite outer surface [49].

3.2. Optical and electrochemical properties

The potential of the as-prepared samples for the light absorption was evaluated using UV–Vis DRS analysis. Fig. 5 (a) clearly shows high UV light harvesting with insignificant visible absorption. However, a wider and more absorption of both visible and UV lights were observed for the M-WO_{3-x}@MC and NM-WO_{3-x}@MC, revealing the formation of extra photo-generated electron-hole pairs, particularly under the visible light wavelengths. The E_g of the samples was estimated via the slops of $(\alpha h\upsilon)^2$ against $h\upsilon$ curves as 2.88, 2.44 and 2.30 eV for the WO_3, M-WO_{3-x}@MC and NM-WO_{3-x}@MC, respectively; where α, h and υ are absorbance coefficient, Planck constant and light frequency, respectively [Fig. 5 (b)] [1]. Three reasons can explain the enhancement of the enhanced light absorption of M-WO_{3-x}@MC. First, the presence of the Fe_3O_4 can change the normal charge-transfer mechanism to Z-scheme photocatalytic procedure, which enhances the harvesting of light, spatially separated oxidative and reductive active sites and capability of the well-preserved strong redox [50]. Second, the MC porous structure with considerable surface area is desirable for subjecting extra active sites to the visible light [51]. Third, partial reduction of WO_3 (confirmed by the XPS and XRD analyses) results in the oxygen vacancies in its structure generating filled impurity band, which remarkably declines the amount of E_g [12]. The same results have been reported by Zhang et al., in which the red-shift of the band edge absorption for the WO_{3-x}/C was observed in comparison to the pristine WO_3, demonstrating that the oxygen vacancies and carbon coating in the WO_{3-x}/C enhance the light absorption and separation of charge carriers considerably [13]. Visible light absorption after nitrogen doping is considerably increased by the NM-WO_{3-x}@MC nanocomposite [Fig. 5 (a)], which is owing to the narrower band gap and consequently, the observed red-shift [52]. Mechanism of the increased light absorption by the N-doped photocatalysts can be explained from the following main point of views [52]: (1) theory of band-gap narrowing: the overlap of O 2p and N 2p orbitals results in the rise of valence-band top;

(2) theory of local energy level: local energy level of N 2p is formed above the valence band leading to the response for visible-light; (3) theory of oxygen vacancy: oxygen vacancy generates the response for visible-light, and the doped-N stabilizes the oxygen vacancy; (4) theory of synergy: the synergy of oxygen vacancies and N 2p local energy levels leads to the visible-light response. Thus, the visible light can be effectively harvested by the N-doped nanocomposite for charge carrier production. Eventually, it should be mentioned that the π-conjugated species like polycyclic aromatic hydrocarbons in the nanocomposite photocatalysts cause the band at approximately 320 nm in the absorption spectra, which is in agreement with the other studies [11].

The behavior of photo-excited charge carriers in photochemical procedures can be appropriately studied by the PL spectroscopy analysis. As seen in Fig. 5 (c), the NM-WO_{3-x}@MC demonstrates the weakest intensity of PL, revealing more efficient inhabitation of the recombination of the electron-hole pair. This indicates that the recombination phenomena were noticeably retarded, and the separation of photogenerated charge carriers is accomplished by the presence of MC and nitrogen doping [40, 53].

The electrochemical impedance spectroscopy (EIS) test was performed to study the electron-transport capacity of the generated materials [Fig. 5 (d)]. Variations in the electrochemical impedance are significant indicators to evaluate the changes in the interfacial properties. A remarkable interfacial transport promotes the charge carrier's separation and consequently declines their recombination, which leads to the decreased impedance in semiconductors. The order of WO_3 > M-WO_{3-x}@MC > NM-WO_{3-x}@MC was obtained for the arc radius of EIS Nyquist plot; its lower amount for a photocatalyst demonstrates faster transportation of the interfacial charge to an acceptor of the electron, which results in efficient separation of the electron-hole pairs [11]. It can be explained by the transportation of the excited electrons in WO_{3-x}, to the mesoporous carbon, inhibiting the rapid electron-hole pairs

recombination. The MC acts as a separation center for the electron-hole pairs due to its conjugated structure [54]. Furthermore, the radius of arc on the EIS spectra also indicates the migration rate happening on the photocatalyst surface and hence, it proposes a more efficient separation of charge carriers under the identical operational condition and quicker transfer of interfacial charges takes place on the surface of NM-WO_{3-x}@MC nanocomposite [55]. The EIS results were simulated properly by an electrical equivalent circuit diagram (inset of Fig. 5d). From this diagram, it can be concluded that all the electrodes are affected by the interfacial charge transfer resistance (R_{ct}), the internal resistance (R_s), the constant phase element (CPE) and the Warburg impedance of diffusive resistance (Z_w), respectively. The R_s and R_{ct} values were obtained from the first intersecting point with the real axis in the high-frequency region and the diameter of the semicircle, respectively (Table S4). Obviously, the NM-WO_{3-x}@MC demonstrates the lower R_{ct} (513 ohm) than the M-WO_{3-x}@MC (757 ohm) and WO_3 (1401 ohm). Hence, the NM-WO_{3-x}@MC possesses a lower resistance for charge separation than that gained in the other materials, consequently indicating an improvement in the charge transfer and separation transfer between the interfaces, which is consistent with previous literature [56].

For more confirmation of the above proposed photocatalytic procedure, the transient photocurrent responses of the samples were examined using typical irradiation with switch on-off cycles. Fig. 5e displays a comparison of photocurrent–time (I–t) plots for the NM-WO_{3-x}@MC, M-WO_{3-x}@MC and WO_3. The photocurrent yielded in three electrodes when the samples were subjected to the visible light, and the photocurrent amount rapidly declined to zero as the irradiation was turned off, which showed the acceptable reproducibility of the samples. The reversible phenomenon of photoresponsivity revealed that the majority of photogenerated electrons were transported to the back contact across the sample to generate the photocurrent under the irradiation. Meanwhile, the NM-WO_{3-x}@MC composite demonstrates the highest photocurrent amount, which is 7.1 and 1.6 times greater than the pure

WO_3 and M-WO_{3-x}@MC, respectively, confirming the better separation rate of photoinduced carriers [11].

Fig. 5 (f) displays the LSV curves for the prepared photocatalysts, in which NM-WO_{3-x}@MC has the most current density with the highest electron migration. A Commercial Pt/C electrode was also applied to compare LSV curves in this study. It is common to utilize the potential value for the generation of 10 mA cm^{-2} current density to determine the electrochemical properties of the photocatalysts [57]. A considerable small overpotential is observed for the maximum activity of the Pt/C electrode (0.08 V vs NHE); the NM-WO_{3-x}@MC overpotential is estimated as 0.16 V against NHE, which is lower than the M-WO_{3-x}@MC and WO_3 (0.23 and 0.35 vs NHE) and nearer to the Pt/C.

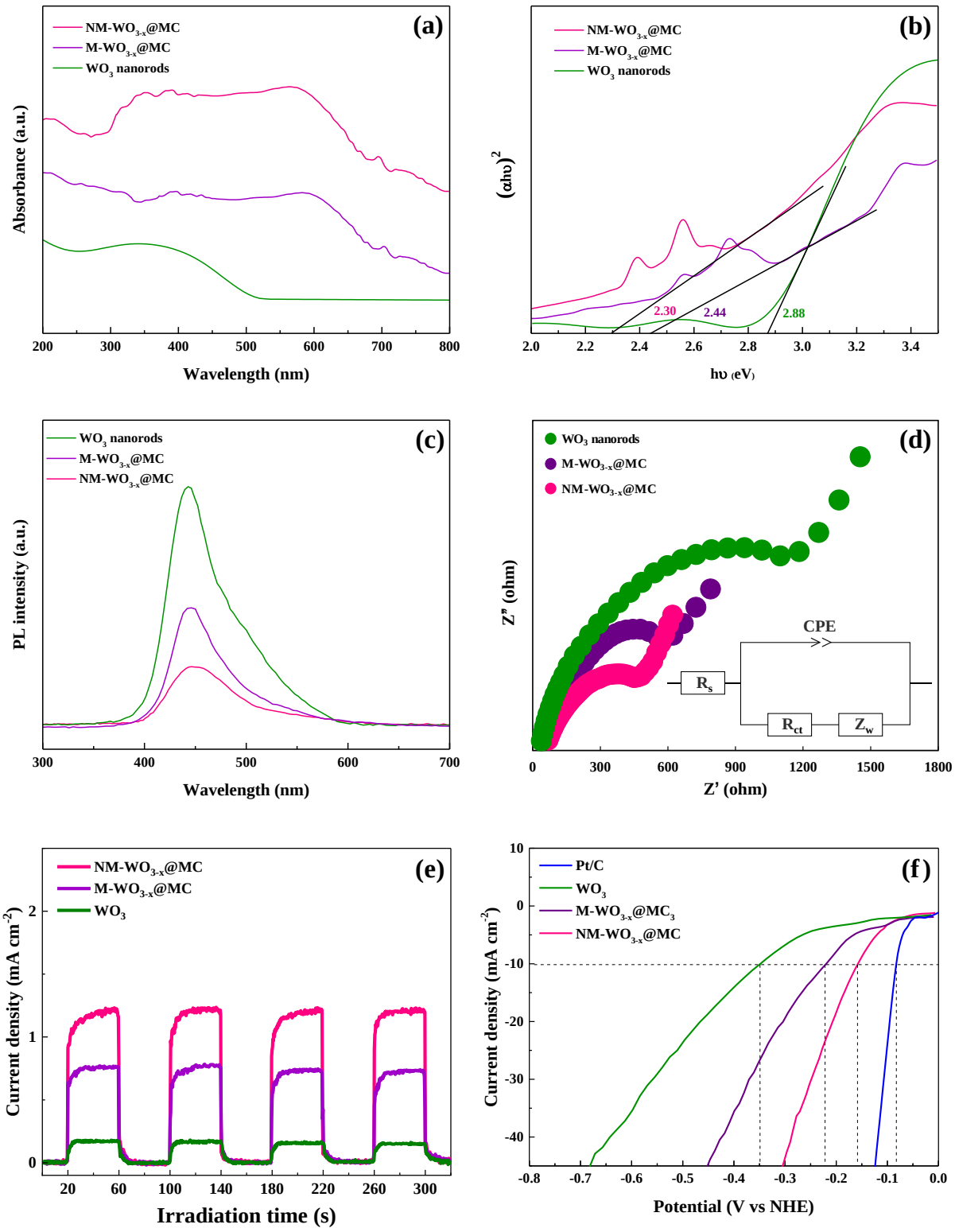

Fig. 5. UV-DRS (a), $(\alpha h\upsilon)^2$-hυ plots (b), PL spectra (c), EIS Nyquist plots (d), transient photocurrent response spectra (e) and LSV curves (f) of WO_3 nanorods, M-WO_{3-x}@MC and NM-WO_{3-x}@MC nanocomposites.

3.3. Photocatalytic H_2 generation

Fig. 6 (a) demonstrates the photocatalytic H_2 generation by the visible light in the presence of WO_3 (532 μmol g^{-1} h^{-1}), M-WO_{3-x}@MC (1569 μmol g^{-1} h^{-1}) and NM-WO_{3-x}@MC (2765 μmol g^{-1} h^{-1}). The low rate for the H_2 formation by the WO_3 can be attributed to the small specific surface area, limited charge transfer and high E_g. Approximately 5-fold enhancement was achieved in the NM-WO_{3-x}@MC activity owing to its extra surface area, light absorption, and electron transfer as well as low recombination of the electron-hole pairs. The AQE of WO_3, M-WO_{3-x}@MC and NM-WO_{3-x}@MC was calculated to be 4.2%, 12.3% and 21.7% at 420 nm, respectively. After excitation of electrons in the valance band (VB) of WO_{3-x} nanorods to form the charge carriers, these photo-generated electrons in the conduction band (CB) can directly migrate to the MC through their solid-solid interface due to its remarkable electron transfer capability. The surface reduction for the H_2 production occurs by these electrons participation [58]. The valance band positions of the WO_3 and Fe_3O_4 were estimated using the VB-XPS by linearly extrapolating the leading edge of valence band XPS curve to the baseline (Fig. S5) as 2.59 eV and 0.81 eV (vs. NHE), respectively. Moreover, the bandgap amounts were calculated optically as 2.88 and 1.76 eV for the WO_3 and Fe_3O_4, respectively. Then, the CB positions can be determined as −0.29 and −0.95 eV (vs. NHE) for the mentioned samples, respectively ($E_{CB} = E_{VB} - E_g$). These results are in good agreement with other studies [59-61]. For the H_2 evolution, the CB position of WO_3 should be more negative than the reduction potential of H^+/H_2 (0 V vs. NHE) and the VB position of WO_3 should be more positive than the oxidation potential of O_2/H_2O (1.23 eV vs. NHE). However, the wide band gap of WO_3 has a wide band gap leads to low absorption of the solar-light. On the other hand, fast recombination of the photogenerated electron-hole pairs also confines the utilization of solar energy [62]. The optically obtained band gaps of the M-WO_{3-x}@MC and NM-WO_{3-x}@MC are estimated as 2.44 and 2.30 eV,

respectively, which are narrower than the pure WO_3. Moreover, the N doping forms a new impurity level above the of WO_3, which explains the lower band gap of the NM-WO_{3-x}@MC compared to the M-WO_{3-x}@MC. Besides, the N-doped mesoporous carbon can be employed as the electron donors and electron acceptors [63]; hence, it accepts the excited electrons from the WO_{3-x} conduction band via the photoinduced charge transfer mechanism and increases the electron-hole pairs life time. It should be noted that the presence of Fe_3O_4 can change the normal charge-transfer mechanism to a Z-scheme, which results in the high reactivity of CB and VB. The schematic diagram for the mechanism of photocatalytic hydrogen production using NM-WO_{3-x}@MC is shown in Fig. S6. Furthermore, the 3D structure of the nanocomposite decreases the charge carriers diffusion length and intensifies its electron transfer on the terminal sites [64]. The improvement in the H_2 production rate of the NM-WO_{3-x}@MC can also be related to its superior absorption ability in the visible region as shown in Fig. 5a. According to the XPS results, the N atoms present in the NM-WO_{3-x}@MC structure increases the oxygen vacancies, which decreases the recombination of electron-holes within the photocatalysis; consequently, this photocatalyst has the highest absorption of visible light, and thus, intensifies the catalytic activity in the visible area. In order to monitor the stabilities of WO_3 and NM-WO_{3-x}@MC within long-term usages for the H_2 formation, the five repeated photocatalytic runs were implemented and the results are shown in Fig. 6 (c). The activity of both photocatalysts demonstrates no significant decrease after the subsequent cycles (total 20 h) confirming their suitable durability for the visible-light-driven H_2 generation. Table S5 compares H_2 production rates and stabilities of NM-WO_{3-x}@MC and other materials reported in the literature. This comparison demonstrates that the nanocomposite fabricated in this study possess higher activity and durability than those of previously reported WO_3-based nanostructures.

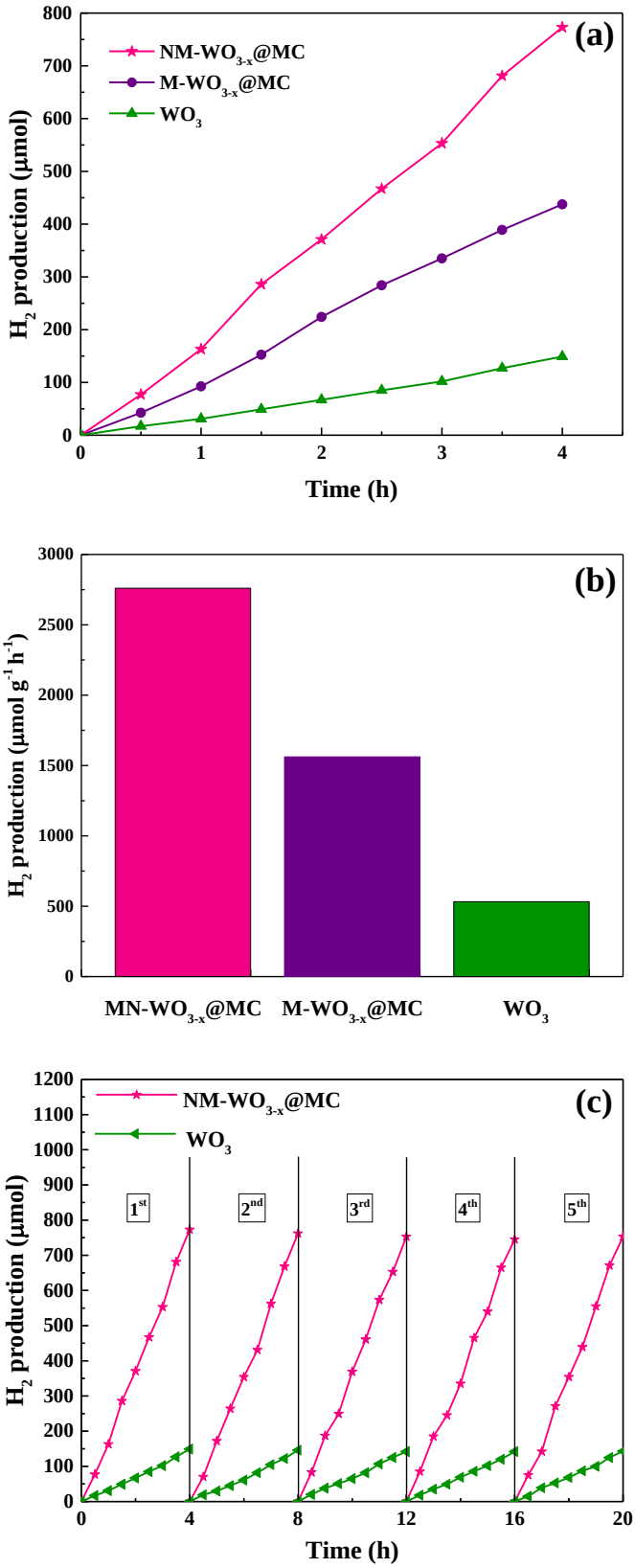

Fig. 6. Time course of hydrogen production (a), corresponding rate comparison (b) and cyclic stability (c) of the photocatalysts; photocatalyst amount= 50 mg.

The used catalyst was characterized to determine the morphological, chemical and structural conversions. The catalyst morphology was characterized by the SEM after its usage. As can be observed in Fig. S7 (a and b), the used catalyst showed no evident morphological difference compared to the fresh catalyst. The XRD (Fig. S8 (a)), Raman (Fig. S8 (b)) and XPS spectra (Fig. S8 (c)), corresponding to the used NM-WO_{3-x}@MC, demonstrated that the crystallinity and chemical structure remained quite stable along the treatment, without any evidence of its change. The W 4f high-resolution spectra of used NM-WO_{3-x}@MC represented that like unused photocatalyst the curve was deconvolved into four peaks at 34.3 ± 0.1, 35.6± 0.1, 36.6± 0.1 and 37.7 ± 0.1 indicating both +6 and +5 oxidation states for the tungsten (Fig. S8 (d)). The N 1s high-resolution spectrum exhibited all of the obtained peaks related to the graphitic nitrogen, pyrrolic nitrogen and pyridinic nitrogen were the same as fresh NM-WO_{3-x}@MC (Fig. S8 (e)).

3.4. Photocatalytic degradation of antibiotics

3.4.1. Comparison of different photocatalysts activities

To further study the photocatalytic activity NM-WO_{3-x}@MC, a number of treatment runs were performed for the cephalexin [Fig. 7 (a)], cefazolin [Fig. 7 (b)] and cephradine [Fig. 7 (c)] antibiotics as model emerging pollutants. Control tests revealed that the adsorption of the antibiotics on NM-WO_{3-x}@MC in the dark was insignificant (less than 17%). Moreover, sole visible light irradiation had a negligible role in the degradation of antibiotics (less than 6%) after 150 min. The pure WO_3 demonstrated low activity for the photocatalysis of cephalexin, cefazolin and cephradine after 120 min under the visible light due to broad band gap and rapid electron and hole recombination [9, 10]. Application of nanocomposite photocatalysts including the M-WO_{3-x}@MC and NM-WO_{3-x}@MC increased the antibiotics degradation under identical

experimental conditions. The M-WO_{3-x}@MC possesses extra active sites to form higher reactive species due to higher specific surface area [1]. The best photocatalytic behavior of NM-WO_{3-x}@MC can be attributed to (1) easier active species formation due to the narrower bandgap and effective visible light-harvesting, (2) special mesoporous structure and crystallinity with the high surface area for proper transportation of reactants to the catalyst site, and (3) appropriate separation of photogenerated electron-hole pairs owing to the above-mentioned synergistic effects [65, 66].

The positions of band edge for the WO_3 and Fe_3O_4 were determined by the VB-XPS (Fig. S5). Clearly, the VB of WO_3 and Fe_3O_4 is 2.59 eV and 0.81 eV (vs. NHE), respectively. Given E_g of the WO_3 nanorods and Fe_3O_4 nanoparticles as 2.88 and 1.76 eV, corresponding E_{CB} could be estimated to be −0.29 and −0.95 eV, respectively, which is consistent with the literature [59-61] The schematic diagram for the mechanism of photocatalytic degradation of the antibiotics using NM-WO_{3-x}@MC is shown in Fig. S9. Under the visible irradiation, the WO_{3-x} gets photo-excited to form charge carriers, which emanate via the electron transfer from the WO_{3-x} valence band to its conduction band. Nitrogen doping produces impurity levels above the WO_{3-x} valence band, absorbing visible light efficiently. The electrons could migrate to the mesoporous carbon surface via the photo-induced charge transfer procedure and therefore, it confines the electron-hole recombination. The NM-WO_{3-x}@MC with a higher surface area and the porous structure is desirable to expose the active sites for adsorption of the H^+ and enhancement of the mass transfer. Furthermore, the CB potential of WO_{3-x} is less positive than the VB potential of Fe_3O_4; hence, the photoexcited electron from the WO_{3-x} can migrate via the Z-scheme photocatalytic system to the Fe_3O_4. It is also proven that the N-doped mesoporous carbon can act as the charge transfer mediator between the WO_{3-x} and Fe_3O_4 [63]. On the other hand, some other parts of the photoinduced electrons from the Fe_3O_4 valance band can transfer to its conduction band to produce the $O_2^{\bullet-}$ while inhibiting the e^-/h^+ recombination by the N-

doped MC. Eventually, the generated reactive h^+ in the WO_{3-x} valance band can also generate the •OH radicals owing to its VB higher potential compared to the OH^-/•OH potential (1.99 eV vs. NHE) [60].

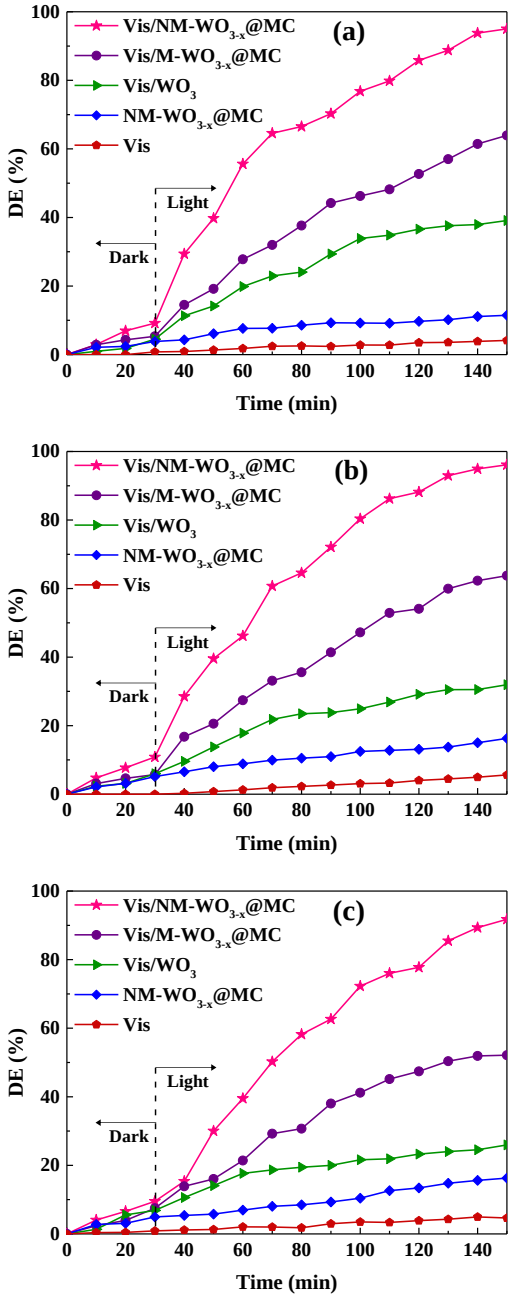

Fig. 7. Comparison of the performance of various photocatalysts in the simultaneous photocatalytic degradation of cephalexin (a), cefazolin (b) and cephradine (c); Experimental conditions: $[pollutant]_0$ = 2 mM, photocatalyst dosage of 0.6 g/L, and pH = 6.7.

3.4.2. Mechanisms and pathways for degradation of antibiotics

Organic scavengers affect the photocatalytic process through the prevention of the oxidizing species reactivity resulting in the restricted antibiotics destruction. To identify the main reactive species that contributed to the antibiotics degradation, scavenging reactions were performed with the photocatalytic treatment using 1,4-benzoquinone (BQ), isopropanol (IPA) and ethylenediaminetetraacetic acid disodium salt (EDTA-2Na) as the scavengers of $O_2^{\bullet-}$, $^{\bullet}OH$ and h^+, respectively [1]. The order of scavenging effect was found to be BQ > IPA > EDTA-2Na, which indicates the substantial role of $O_2^{\bullet-}$ radicals in the photocatalytic degradation of cephalexin [Fig. 8 (a)], cefazolin [Fig. 8 (b)] and cephradine [Fig. 8 (c)] antibiotics. The formation of the reactive oxygen species was confirmed via the ESR spin trapping method. The obtained ESR signals for the DMPO–$O_2^{\bullet-}$ are more than the DMPO–$^{\bullet}OH$, which also verify the main function of superoxide during the antibiotics photodegradation.

The GC-MS was utilized to determine the by-products of contaminants degradation using the NM-WO_{3-x}@MC catalyst. Identified structures of the intermediates are listed in Tables S6-S8, and the plausible pathways for the degradation of cephalexin, cefazolin and cephradine are presented in Figs. S10-S12, respectively. For the cephalexin, eight by-products were identified with various retention times (min) and fragments and the related degradation pathway is displayed in Fig. S10. In the beginning, the cephalexin was reacted with the active species, resulting in the production of (2S)-2-amino-N-methyl-2-phenylacetamide, 2,4-azetidinedione (azo-heterocyclic substance) and 3-methylbut-2-enoic acid (unsaturated acid). Afterward, the (2S)-2-amino-N-methyl-2-phenylacetamide undergoes deamination and more oxidation, producing 2-amino-2-hydroxyacetamide and 1,4-benzoquinone. The 1,4-benzoquinone then experienced ring-opening oxidation to form (Z)-but-2-enedioic acid. Moreover, the subsequent loss of NH in 2,4-azetidinedione resulted in the heterocycle cleavage, producing (Z)-but-2-

enedioic acid through more oxidation. The C=C bond of 3-methylbut-2-enoic acid was attacked by addition reactions and as a consequence, the saturated 2-hydroxy-3-methylbutanoic acid was generated.

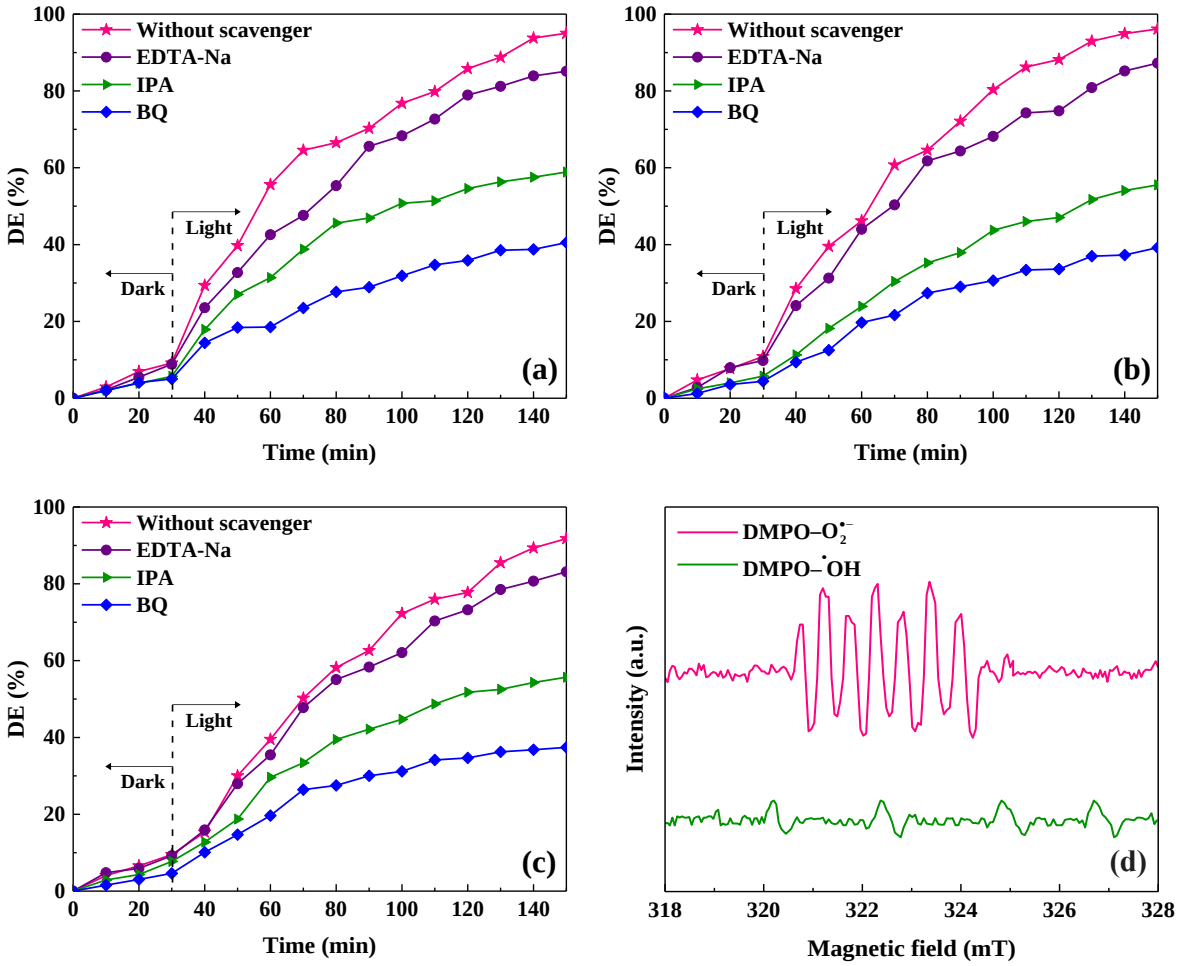

Fig. 8. Effect of different scavengers on the degradation of cephalexin (a), cefazolin (b), cephradine (c), and ESR spectra of DMPO–$O_2^{\bullet-}$ and DMPO–$^{\bullet}$OH (b); Experimental conditions: photocatalyst dosage of 0.7 g/L, $[pollutant]_0$ = 2 mM, pH = 6.7 and [scavenger] = 20 mM.

For the cefazolin, the N-C and N-N bonds cleavage can be considered as the early steps of the degradation reactions leading to the β-lactam ring opening to form the five-membered aliphatic and aromatic rings with S and N heteroatoms. The complexity of cefazolin degradation is confirmed by the formation of various cyclic compounds. According to the recognized intermediates, three degradation routes were proposed for the conversion of cefazolin (Fig. S11). In the first route, the cefazolin was destructed to 2-[(5-methyl-1,3,4-thiadiazol-2-yl)sulfanyl]acetic acid and then, to 5-methyl-1,3,4-thiadiazol-2(3H)-one. In the next step, the 5-methyl-1,3,4-thiadiazol-2(3H)-one was changed to the carboxylic acids and aliphatic compounds such as 2-hydroxypropanehydrazide. In the second pathway, the contaminant was degraded to 3-methyl-1,3-thiazinane-4-carboxylic acid and next to (4S)-3-acetyl-1,3-thiazolidine-4-carboxylic acid. Then, the (4S)-3-Acetyl-1,3-thiazolidine-4-carboxylic acid was degraded to aliphatic compounds such as (2S)-3-Hydroxy-2-(methylamino)propanoic acid. In the initial step of the last pathway, N-(2,2-dihydroxyethyl)-2-(tetrazol-1-yl)acetamide was formed and then destructed to 2-(tetrazol-1-yl)acetic acid and 2-aminoacetic acid; then, these two by-products were degraded to 2H-tetrazole and oxalic acid. The destruction route of cephradine (Fig. S12) was similar to the cephalexin (Fig. S10); however, a difference was observed between the degradation of cephalexin aromatic ring and cephradine 1,4-cyclodihexene ring. For the cephradine, (2S)-2-amino-N-methyl-2-(1,4-cyclohexadiene)acetamide was directly degraded to 2-aminooctanoic acid and then smaller amides and aliphatic carboxylic acids such as 2-amino-2- hydroxyacetamide and hexanoic acid. For all the contaminates, the as-generated aliphatic compounds and carboxylic acids were destructed to low-carbon-content aliphatics and finally converted to the inorganic ions, carbon dioxide and water for their complete mineralization. Eventually, it should be noticed that there were other by-products generated from the degradation of the antibiotic, which could not be identified owing to their short life-time or their low match factor.

The TOC and IC runs were carried out to determine the capability of the NM-WO_{3-x}@MC for the mineralization of the antibiotics. The outcomes gained from the TOC analysis reveals the TOC elimination of 53% and 76% after 120 and 240 min, respectively, under the optimized conditions. Furthermore, based on the IC data, the concentrations of NO_3^-, NH_4^+ and SO_4^{2-} enhanced from 0.9, 0.4 and 0.7 mg L^{-1} to 7.3, 3.9 and 6.4 mg L^{-1} after 120 min of the treatment. This demonstrates the formation of ionic species from antibiotics destruction. A decrease of the TOC amount in addition to the release of nitrogen and sulfur products within the treatment procedure confirms the efficient contaminants mineralization.

4. Conclusions

This study demonstrated a method for the preparation of the durable and high-efficient photocatalyst using the diatom template. for energy production and environmental protection. The magnetic diatom frustules were successfully applied to prepare a highly ordered photocatalyst, in which the reduced tungsten oxide was embedded into mesoporous carbon (M-WO_{3-x}@MC) via the one-pot evaporation-induced self-assembly procedure. The M-WO_{3-x}@MC was then treated by the non-thermal plasma using the N_2 gas to obtain the N-doped catalyst (NM-WO_{3-x}@MC). The XPS and XRD results confirmed successful preparation of NM-WO_{3-x}@MC nanocomposite as well as the WO_3 nanorods, which was then partially reduced by the resol in the nanocomposites. The specific structure of the diatom frustule could prevent the NM-WO_{3-x}@MC from aggregation and consequently its accessible surface area and active sites enhanced considerably. The EIS and PL results revealed that the e/h^+ recombination was remarkably prohibited by the combination of both N-doped mesoporous carbon and reduced tungsten oxide. The band gap of M-WO_{3-x}@MC and NM-WO_{3-x}@MC nanocomposites was estimated as 2.44 and 2.30 eV, respectively; These values were lower than

WO_3 band gap (~2.8 eV), which could be excited by the visible light efficiently. NM-WO_{3-x}@MC showed the highest hydrogen formation rate of 2765 μmol g^{-1} h^{-1}, which was approximately 5 folds greater than that of the WO_3 nanorods (532 μmol g^{-1} h^{-1}). The $O_2^{\bullet-}$ radicals were discovered to have a significant role in the degradation of the antibiotics by the implementation of the scavenging runs and ESR analysis. Eventually, it could be concluded that the NM-WO_{3-x}@MC photocatalyst had the advantage for the β-lactam antibiotics destruction and mineralization, as the EISA procedure and plasma treatment were involved as the simple and practical methods as well as using the low-cost diatom frustule as the natural template.

Supporting Information

Brief statement in nonsentence format listing the contents of the material supplied as Supporting Information.

Acknowledgments

The authors wish to thank the University of Tabriz and University of Eastern Finland for their support. P. Gholami also gratefully acknowledges Centre for International Mobility (CIMO), Finland for providing EDUFI fellowship (decision number TM-18-10895). This paper has been supported by the RUDN University Strategic Academic Leadership Program.

References

1. Kumar, A.; Rana, A.; Sharma, G.; Naushad, M.; Al-Muhtaseb, A. a. H.; Guo, C.; Iglesias-Juez, A.; Stadler, F. J., High-Performance Photocatalytic Hydrogen Production and

Degradation of Levofloxacin by Wide Spectrum-Responsive Ag/Fe_3O_4 Bridged $SrTiO_3$/g-C_3N_4 Plasmonic Nanojunctions: Joint Effect of Ag and Fe_3O_4. *ACS Appl. Mater. Interfaces* **2018,** *10* (47), 40474-40490.

2. Ren, L.; Tong, L.; Yi, X.; Zhou, W.; Wang, D.; Liu, L.; Ye, J., Ultrathin Graphene Encapsulated Cu Nanoparticles: A Highly Stable and Efficient Catalyst for Photocatalytic H_2 Evolution and Degradation of Isopropanol. *Chem. Eng. J.* **2020,** *390*, 124558.

3. Kuang, P.; Sayed, M.; Fan, J.; Cheng, B.; Yu, J., 3d Graphene-Based H_2-Production Photocatalyst and Electrocatalyst. *Adv. Energy Mater.* **2020,** *10* (14), 1903802.

4. Lin, X.; Xu, J.; Keller, A. A.; He, L.; Gu, Y.; Zheng, W.; Sun, D.; Lu, Z.; Huang, J.; Huang, X.; Li, G., Occurrence and Risk Assessment of Emerging Contaminants in a Water Reclamation and Ecological Reuse Project. *Sci. Total Environ.* **2020,** *744*, 140977.

5. Chen, D.; Li, B.; Pu, Q.; Chen, X.; Wen, G.; Li, Z., Preparation of Ag-$AgVO_3$/g-C_3N_4 Composite Photo-Catalyst and Degradation Characteristics of Antibiotics. *J. Hazard. Mater.* **2019,** *373*, 303-312.

6. Zhang, H.; Song, Y.; Nengzi, L.-c.; Gou, J.; Li, B.; Cheng, X., Activation of Persulfate by a Novel Magnetic $CuFe_2O_4$/Bi_2O_3 Composite for Lomefloxacin Degradation. *Chem. Eng. J.* **2020,** *379*, 122362.

7. Orooji, Y.; Ghanbari, M.; Amiri, O.; Salavati-Niasari, M., Facile Fabrication of Silver Iodide/Graphitic Carbon Nitride Nanocomposites by Notable Photo-Catalytic Performance through Sunlight and Antimicrobial Activity. *J. Hazard. Mater.* **2020,** *389*, 122079.

8. Li, B.; Lai, C.; Zeng, G.; Qin, L.; Yi, H.; Huang, D.; Zhou, C.; Liu, X.; Cheng, M.; Xu, P.; Zhang, C.; Huang, F.; Liu, S., Facile Hydrothermal Synthesis of Z-Scheme $Bi_2Fe_4O_9$/Bi_2WO_6 Heterojunction Photocatalyst with Enhanced Visible Light Photocatalytic Activity. *ACS Appl. Mater. Interfaces* **2018,** *10* (22), 18824-18836.

9. Mojaddami, M.; Simchi, A., Robust Water Splitting on Staggered Gap Heterojunctions Based on WO_3\WS_2–MoS_2 Nanostructures. *Renewable Energy* **2020,** *162*, 504-512.

10. Jamila, G. S.; Sajjad, S.; Leghari, S. A. K.; Long, M., Nitrogen Doped Carbon Quantum Dots and Go Modified WO_3 Nanosheets Combination as an Effective Visible Photo Catalyst. *J. Hazard. Mater.* **2020,** *382*, 121087.

11. Zhang, J.; Ma, Y.; Du, Y.; Jiang, H.; Zhou, D.; Dong, S., Carbon Nanodots/WO_3 Nanorods Z-Scheme Composites: Remarkably Enhanced Photocatalytic Performance under Broad Spectrum. *Appl. Catal., B* **2017,** *209*, 253-264.

12. Wang, L.; Xu, X.; Wu, S.; Cao, F., Nonstoichiometric Tungsten Oxide Residing in a 3d Nitrogen Doped Carbon Matrix, a Composite Photocatalyst for Oxygen Vacancy Induced Voc Degradation and H_2 Production. *Catal. Sci. Technol.* **2018,** *8* (5), 1366-1374.

13. Zhang, R.; Song, C.; Kou, M.; Yin, P.; Jin, X.; Wang, L.; Deng, Y.; Wang, B.; Xia, D.; Wong, P. K.; Ye, L., Sterilization of Escherichia Coli by Photothermal Synergy of WO_{3-x}/C Nanosheet under Infrared Light Irradiation. *Environ. Sci. Technol.* **2020,** *54* (6), 3691-3701.

14. Li, K.; Liu, X.; Zheng, T.; Jiang, D.; Zhou, Z.; Liu, C.; Zhang, X.; Zhang, Y.; Losic, D., Tuning MnO_2 to Feooh Replicas with Bio-Template 3D Morphology as Electrodes for High Performance Asymmetric Supercapacitors. *Chem. Eng. J.* **2019,** *370*, 136-147.

15. Miao, X.; Yue, X.; Ji, Z.; Shen, X.; Zhou, H.; Liu, M.; Xu, K.; Zhu, J.; Zhu, G.; Kong, L.; Shah, S. A., Nitrogen-Doped Carbon Dots Decorated on g-C_3N_4/Ag_3PO_4 Photocatalyst with Improved Visible Light Photocatalytic Activity and Mechanism Insight. *Appl. Catal., B* **2018,** *227*, 459-469.

16. Daiyan, R.; Zhu, X.; Tong, Z.; Gong, L.; Razmjou, A.; Liu, R.-S.; Xia, Z.; Lu, X.; Dai, L.; Amal, R., Transforming Active Sites in Nickel–Nitrogen–Carbon Catalysts for Efficient Electrochemical CO_2 Reduction to CO. *Nano Energy* **2020,** *78*, 105213.

17. Kaur, N.; Shahi, S. K.; Shahi, J. S.; Sandhu, S.; Sharma, R.; Singh, V., Comprehensive Review and Future Perspectives of Efficient N-Doped, Fe-Doped and (N,Fe)-Co-Doped Titania as Visible Light Active Photocatalysts. *Vacuum* **2020,** *178*, 109429.

18. Azcatl, A.; Qin, X.; Prakash, A.; Zhang, C.; Cheng, L.; Wang, Q.; Lu, N.; Kim, M. J.; Kim, J.; Cho, K.; Addou, R.; Hinkle, C. L.; Appenzeller, J.; Wallace, R. M., Covalent Nitrogen Doping and Compressive Strain in MoS_2 by Remote N_2 Plasma Exposure. *Nano Lett.* **2016,** *16* (9), 5437-5443.

19. Akada, K.; Terasawa, T.-O.; Imamura, G.; Obata, S.; Saiki, K., Control of Work Function of Graphene by Plasma Assisted Nitrogen Doping. *Appl. Phys. Lett.* **2014,** *104* (13), 131602.

20. Patel, P.; Nadesalingam, M.; Wallace, R.; Buchanan, D., Physical and Optoelectronic Characterization of Reactively Sputtered Molybdenum-Silicon-Nitride Alloy Metal Gate Electrodes. *J. Appl. Phys.* **2009,** *105* (2), 024517.

21. Gholami, P.; Khataee, A.; Bhatnagar, A., Environmentally Superior Cleaning of Diatom Frustules Using Sono-Fenton Process: Facile Fabrication of Nanoporous Silica with Homogeneous Morphology and Controlled Size. *Ultrason. Sonochem.* **2020,** *64*, 105044.

22. Gholami, P.; Khataee, A.; Vahid, B., Integration of Polydopamine and Fe_3O_4 Nanoparticles with Graphene Oxide to Fabricate an Efficient Recoverable Catalyst for the Degradation of Sulfadiazine. *Ind. Eng. Chem. Res.* **2020,** *59* (1), 183-193.

23. Gholami, P.; Khataee, A.; Bhatnagar, A., Photocatalytic Degradation of Antibiotic and Hydrogen Production Using Diatom-Templated 3D Wo_{3-X}@Mesoporous Carbon Nanohybrid under Visible Light Irradiation. *J. Cleaner Prod.* **2020,** *275*, 124157.

24. Jo, C.; Hwang, J.; Song, H.; Dao, A. H.; Kim, Y.-T.; Lee, S. H.; Hong, S. W.; Yoon, S.; Lee, J., Block-Copolymer-Assisted One-Pot Synthesis of Ordered Mesoporous

Wo_{3-X}/Carbon Nanocomposites as High-Rate-Performance Electrodes for Pseudocapacitors. *Adv. Funct. Mater.* **2013,** *23* (30), 3747-3754.

25. Luo, M.; Yang, Q.; Yang, W.; Wang, J.; He, F.; Liu, K.; Cao, H.; Yan, H., Defects Engineering Leads to Enhanced Photocatalytic H_2 Evolution on Graphitic Carbon Nitride–Covalent Organic Framework Nanosheet Composite. *Small* **2020,** *16* (20), 2001100.

26. Farag, S. A., Simultaneous Liquid Chromatographic Analysis of the *β-Lactam* Antibiotics Cefazolin, Cefadroxil, Cephalexin, Ampicillin, and Cephradine in Solution. *J. AOAC Int.* **1998,** *81* (2), 381-385.

27. Gholizadeh, A. M.; Zarei, M.; Ebratkhahan, M.; Hasanzadeh, A., Phenazopyridine Degradation by Electro-Fenton Process with Magnetite Nanoparticles-Activated Carbon Cathode, Artificial Neural Networks Modeling. *J. Environ. Chem. Eng.* **2021,** *9* (1), 104999.

28. Chandra, D.; Li, D.; Sato, T.; Tanahashi, Y.; Togashi, T.; Ishizaki, M.; Kurihara, M.; Mohamed, E. A.; Tsubonouchi, Y.; Zahran, Z. N.; Saito, K.; Yui, T.; Yagi, M., Characterization and Mechanism of Efficient Visible-Light-Driven Water Oxidation on an in Situ N2-Intercalated WO_3 Nanorod Photoanode. *ACS Sustainable Chem. Eng.* **2019,** *7* (21), 17896-17906.

29. Li, Y.; Fu, Y.; Chen, S.; Huang, Z.; Wang, L.; Song, Y., Porous Fe_2O_3/Fe_3O_4@Carbon Octahedron Arrayed on Three-Dimensional Graphene Foam for Lithium-Ion Battery. *Composites, Part B* **2019,** *171*, 130-137.

30. Lin, J.; Jia, H.; Cai, Y.; Chen, S.; Liang, H.; Wang, X.; Zhang, F.; Qi, J.; Cao, J.; Feng, J.; Fei, W.-d., Modifying the Electrochemical Performance of Vertically-Oriented Few-Layered Graphene through Rotary Plasma Processing. *J. Mater. Chem. A* **2018,** *6* (3), 908-917.

31. Li, Y.; Yan, P.; Chen, J.; Ren, Y.; Zhou, Y.; Ge, T.; Chen, J.; Xu, Q., High-Efficiency Electrocatalyst for N_2 Conversion to NH_3 Based on Au Nanoparticles Loaded on Defective WO_{3-X}. *Chem. Commun.* **2019,** *55* (88), 13307-13310.

32. Taherian, Z.; Khataee, A.; Orooji, Y., Promoted Nickel-Based Catalysts on Modified Mesoporous Silica Support: The Role of Yttria and Magnesia on CO_2 Methanation. *Microporous Mesoporous Mater.* **2020,** *306*, 110455.

33. Nowak, A. P.; Sprynskyy, M.; Brzozowska, W.; Lisowska-Oleksiak, A., Electrochemical Behavior of a Composite Material Containing 3D-Structured Diatom Biosilica. *Algal Res.* **2019,** *41*, 101538.

34. Fathi, Z.; Doustkhah, E.; Rostamnia, S.; Darvishi, F.; Ghodsi, A.; Ide, Y., Interaction of Yarrowia Lipolytica Lipase with Dithiocarbamate Modified Magnetic Carbon Fe_3O_4@ C-$NHCS_2H$ Core-Shell Nanoparticles. *Int. J. Biol. Macromol.* **2018,** *117*, 218-224.

35. Tu, J.; Lei, H.; Yu, Z.; Jiao, S., Ordered WO_{3-X} Nanorods: Facile Synthesis and Their Electrochemical Properties for Aluminum-Ion Batteries. *Chem. Commun.* **2018,** *54* (11), 1343-1346.

36. Choi, J.-H.; Kim, Y.; Kim, B.-s., Multifunctional Role of Reduced Graphene Oxide Binder for High Performance Supercapacitor with Commercial-Level Mass Loading. *J. Power Sources* **2020,** *454*, 227917.

37. Li, Y.; Zhou, X.; Luo, W.; Cheng, X.; Zhu, Y.; El-Toni, A. M.; Khan, A.; Deng, Y.; Zhao, D., Pore Engineering of Mesoporous Tungsten Oxides for Ultrasensitive Gas Sensing. *Adv. Mater. Interfaces* **2019,** *6* (1), 1801269.

38. Cullity, B. D., Elements of X-Ray Diffraction. *Addison-Wesley Publishing*: 1956.

39. Hu, P.; Long, M.; Bai, X.; Wang, C.; Cai, C.; Fu, J.; Zhou, B.; Zhou, Y., Monolithic Cobalt-Doped Carbon Aerogel for Efficient Catalytic Activation of Peroxymonosulfate in Water. *J. Hazard. Mater.* **2017,** *332*, 195-204.

40. Zhan, F.; Liu, Y.; Wang, K.; Yang, X.; Liu, M.; Qiu, X.; Li, J.; Li, W., Oxygen-Deficient Nanofiber WO_{3-X}/Wo_3 Homojunction Photoanodes Synthesized Via a Novel Metal Self-Reducing Method. *ACS Appl. Mater. Interfaces* **2019,** *11* (43), 39951-39960.

41. Rybin, M.; Pereyaslavtsev, A.; Vasilieva, T.; Myasnikov, V.; Sokolov, I.; Pavlova, A.; Obraztsova, E.; Khomich, A.; Ralchenko, V.; Obraztsova, E., Efficient Nitrogen Doping of Graphene by Plasma Treatment. *Carbon* **2016,** *96*, 196-202.

42. Yen, P.-J.; Ting, C.-C.; Chiu, Y.-C.; Tseng, T.-Y.; Hsu, Y.-J.; Wu, W.-W.; Wei, K.-H., Facile Production of Graphene Nanosheets Comprising Nitrogen-Doping through in Situ Cathodic Plasma Formation During Electrochemical Exfoliation. *J. Mater. Chem. C* **2017,** *5* (10), 2597-2602.

43. Lu, Y.-F.; Lo, S.-T.; Lin, J.-C.; Zhang, W.; Lu, J.-Y.; Liu, F.-H.; Tseng, C.-M.; Lee, Y.-H.; Liang, C.-T.; Li, L.-J., Nitrogen-Doped Graphene Sheets Grown by Chemical Vapor Deposition: Synthesis and Influence of Nitrogen Impurities on Carrier Transport. *ACS nano* **2013,** *7* (8), 6522-6532.

44. Yan, J.; Wang, T.; Wu, G.; Dai, W.; Guan, N.; Li, L.; Gong, J., Tungsten Oxide Single Crystal Nanosheets for Enhanced Multichannel Solar Light Harvesting. *Adv. Mater.* **2015,** *27* (9), 1580-1586.

45. Pervez, S. A.; Kim, D.; Doh, C.-H.; Farooq, U.; Choi, H.-Y.; Choi, J.-H., Anodic WO_3 Mesosponge@Carbon: A Novel Binder-Less Electrode for Advanced Energy Storage Devices. *ACS Appl. Mater. Interfaces* **2015,** *7* (14), 7635-7643.

46. Kong, N.; Jia, M.; Yang, C.; Lan, J.; Yu, Y.; Yang, X., Encapsulating V_2O_3 Nanoparticles in Carbon Nanofibers with Internal Void Spaces for a Self-Supported Anode Material in Superior Lithium-Ion Capacitors. *ACS Sustainable Chem. Eng.* **2019,** *7* (24), 19483-19495.

47. Qayyum, A.; Zeb, S.; Ali, S.; Waheed, A.; Zakaullah, M., Optical Emission Spectroscopy of Abnormal Glow Region in Nitrogen Plasma. *Plasma Chem. Plasma Process.* **2005,** *25* (5), 551-564.

48. Klyui, N. I.; Piryatinskii, Y. P.; Semenovich, V. A., Intensive Visible Photoluminescence of a-C:H:N Films. *Mater. Lett.* **1998,** *35* (5), 334-338.

49. Ouyang, B.; Zhang, Y.; Wang, Y.; Zhang, Z.; Fan, H. J.; Rawat, R. S., Plasma Surface Functionalization Induces Nanostructuring and Nitrogen-Doping in Carbon Cloth with Enhanced Energy Storage Performance. *J. Mater. Chem. A* **2016,** *4* (45), 17801-17808.

50. Zhang, H.; Gu, Q.-Q.; Zhou, Y.-W.; Liu, S.-Q.; Liu, W.-X.; Luo, L.; Meng, Z.-D., Direct Z-Scheme Photocatalytic Removal of Ammonia Via the Narrow Band Gap Mos_2/N-Doped Graphene Hybrid Catalyst Upon near-Infrared Irradiation. *Appl. Surf. Sci.* **2020,** *504*, 144065.

51. Hou, D.; Hu, X.; Ho, W.; Hu, P.; Huang, Y., Facile Fabrication of Porous Cr-Doped $Srtio_3$ Nanotubes by Electrospinning and Their Enhanced Visible-Light-Driven Photocatalytic Properties. *J. Mater. Chem. A* **2015,** *3* (7), 3935-3943.

52. Zhao, W.; Liu, S.; Zhang, S.; Wang, R.; Wang, K., Preparation and Visible-Light Photocatalytic Activity of N-Doped TiO_2 by Plasma-Assisted Sol-Gel Method. *Catal. Today* **2019,** *337*, 37-43.

53. Ibukun, O.; Jeong, H. K., Enhancement of Photocatalytic Activities of Nitrogen-Doped Titanium Dioxide by Ambient Plasma. *Chem. Phys. Lett.* **2020,** *744*, 137234.

54. Yang, C.; Cheng, J.; Chen, Y.; Hu, Y., CdS Nanoparticles Immobilized on Porous Carbon Polyhedrons Derived from a Metal-Organic Framework with Enhanced Visible Light Photocatalytic Activity for Antibiotic Degradation. *Appl. Surf. Sci.* **2017,** *420*, 252-259.

55. Hu, S.; Li, F.; Fan, Z.; Gui, J., Improved Photocatalytic Hydrogen Production Property over Ni/NiO/N–TiO_2−X Heterojunction Nanocomposite Prepared by NH_3 Plasma Treatment. *J. Power Sources* **2014,** *250*, 30-39.

56. Tang, Y.; Mak, C. H.; Liu, R.; Wang, Z.; Ji, L.; Song, H.; Tan, C.; Barrière, F.; Hsu, H.-Y., In Situ Formation of Bismuth-Based Perovskite Heterostructures for High-Performance Cocatalyst-Free Photocatalytic Hydrogen Evolution. *Adv. Funct. Mater*. **2020,** *30* (52), 2006919.

57. Zhao, S.; Li, C.; Wang, L.; Liu, N.; Qiao, S.; Liu, B.; Huang, H.; Liu, Y.; Kang, Z., Carbon Quantum Dots Modified MoS_2 with Visible-Light-Induced High Hydrogen Evolution Catalytic Ability. *Carbon* **2016,** *99*, 599-606.

58. Kailasam, K.; Fischer, A.; Zhang, G.; Zhang, J.; Schwarze, M.; Schröder, M.; Wang, X.; Schomäcker, R.; Thomas, A., Mesoporous Carbon Nitride-Tungsten Oxide Composites for Enhanced Photocatalytic Hydrogen Evolution. *ChemSusChem* **2015,** *8* (8), 1404-1410.

59. Niu, H.; Yang, Y.; Zhao, W.; Lv, H.; Zhang, H.; Cai, Y., Single-Crystalline Fe_7S_8/Fe_3O_4 Coated Zero-Valent Iron Synthesized with Vacuum Chemical Vapor Deposition Technique: Enhanced Reductive, Oxidative and Photocatalytic Activity for Water Purification. *J. Hazard. Mater.* **2021,** *401*, 123442.

60. Talukdar, K.; Jun, B.-M.; Yoon, Y.; Kim, Y.; Fayyaz, A.; Park, C. M., Novel Z-Scheme Ag_3PO_4/Fe_3O_4-Activated Biochar Photocatalyst with Enhanced Visible-Light Catalytic Performance toward Degradation of Bisphenol A. *J. Hazard. Mater.* **2020,** *398*, 123025.

61. Zhang, X.; Hao, W.; Tsang, C.-S.; Liu, M.; Hwang, G. S.; Lee, L. Y. S., Psesudocubic Phase Tungsten Oxide as a Photocatalyst for Hydrogen Evolution Reaction. *ACS Appl. Energy Mater.* **2019,** *2* (12), 8792-8800.

62. Du, H.; Liu, Y.-N.; Shen, C.-C.; Xu, A.-W., Nanoheterostructured Photocatalysts for Improving Photocatalytic Hydrogen Production. *Chin. J. Catal.* **2017,** *38* (8), 1295-1306.

63. Qiu, H.-B.; Guo, P.-C.; Yuan, L.; Sheng, G.-P., Different Non-Radical Oxidation Processes of Persulfate and Peroxymonosulfate Activation by Nitrogen-Doped Mesoporous Carbon. *Chin. Chem. Lett.* **2020,** *31* (10), 2614-2618.

64. Wan, S.; Ou, M.; Zhong, Q.; Cai, W., Haloid Acid Induced Carbon Nitride Semiconductors for Enhanced Photocatalytic H_2 Evolution and Reduction of CO_2 under Visible Light. *Carbon* **2018,** *138*, 465-474.

65. Jia, T.; Fu, F.; Yu, D.; Cao, J.; Sun, G., Facile Synthesis and Characterization of N-Doped TiO_2/C Nanocomposites with Enhanced Visible-Light Photocatalytic Performance. *Appl. Surf. Sci.* **2018,** *430*, 438-447.

66. Suresh, S. P.; Lekshmi, G. S.; Kirupha, S. D.; Ariraman, M.; Bazaka, O.; Levchenko, I.; Bazaka, K.; Mandhakini, M., Superhydrophobic Fluorine-Modified Cerium-Doped Mesoporous Carbon as an Efficient Catalytic Platform for Photo-Degradation of Organic Pollutants. *Carbon* **2019,** *147*, 323-333.

Table of Contents Graphic

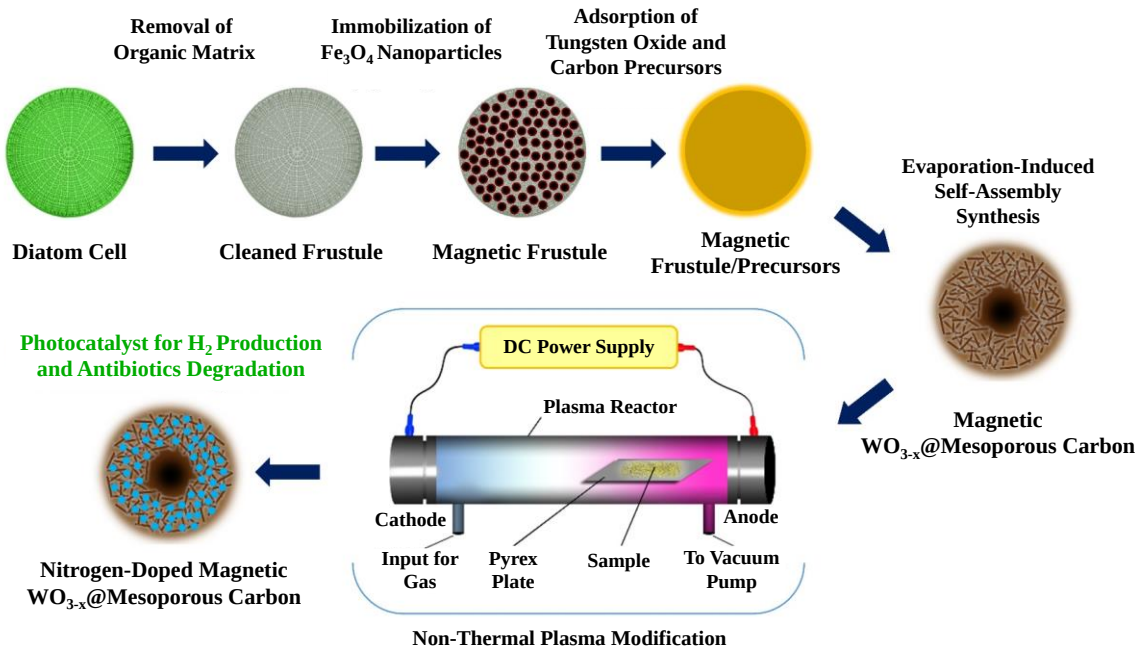

Preparation of nitrogen-doped magnetic WO_{3-x}@mesoporous carbon for photocatalytic H_2 production and antibiotics degradation.